Natural Hazards (2026) 122:127
https://doi.org/10.1007/s11069-025-07880-2

ORIGINAL PAPER

Geomorphological and sedimentological traces of the 365 AD and 1303 AD tsunami impacts on the Korission Lagoon (Corfu Island, Greece) compared with tsunami simulation scenarios

Tina Georg[1,2] · **Björn R. Röbke**[3] · **Peter Fischer**[1] · **Peter Frenzel**[4] · **Kalliopi Baika**[5] · **Timo Willershäuser**[1] · **Andreas Vött**[1]

Received: 12 May 2025 / Accepted: 1 October 2025

Abstract
The AD 365 and the AD 1303 tsunamis are known extreme wave events that caused severe damage and fatalities along the coastlines of the eastern Mediterranean Sea. We analysed geomorphological and sedimentological data from the Korission Lagoon (Corfu Island, Greece) and compared them with results of numerical simulations. Washover fans and sediment cores reveal coarse-grained high-energy deposits intersecting prevailing lagoonal conditions. Geochemical and microfaunal analyses document a marine origin of these deposits. Results of radiocarbon dating suggest that they may correlate with the 365 AD and 1303 AD tsunami events. Numerical simulations of the 365 AD tsunami suggest the formation of several generations of tsunami waves during tsunami landfall. Erosion of the beach ridge and sedimentation in the lagoon increases with higher tsunami wave heights and flow velocities and is strongly controlled by the local topography. Generally, we found good agreement between field data and numerical simulation. Our model validation allows to investigate the morphodynamic response of the 365 AD tsunami along other coastlines of Greece. The current study demonstrates that numerical morphodynamic models can successfully be applied for a comparison with historical tsunami events, if tsunami deposits are well-preserved and sufficient information on the tsunami trigger mechanism is available.

Keywords 365 AD · 1303 AD · Earthquake · Tsunami · Numerical simulation · Coastal geomorphology

1 Introduction

The eastern Mediterranean Sea is a region of high seismic activity due to the collision of the African and Eurasian plates. Along the Hellenic Arc, the African plate is being subducted beneath the Eurasian plate causing the strongest earthquakes in the Mediterranean

Extended author information available on the last page of the article

Published online: 06 February 2026

Sea (Fig. 1). Although few hundred kilometres distant from the Hellenic Arc, the island of Corfu—the northernmost Ionian Island—is subject to high seismicity. In 2024, more than 600 earthquakes of $M_S >= 3.5$ were recorded in a range of 600 km around Corfu Island which also includes the Hellenic Trench near Crete Island (International Seismological Centre 2025). With their ground movements, earthquakes can trigger tsunamis if they occur in offshore areas. In fact, seismicity is the main trigger of tsunamis but not all earthquakes are tsunamigenic (Röbke and Vött 2017). Among other factors, a threshold of $M_S = 6.5$ of an offshore earthquake is considered to be needed to cause tsunamis (Röbke and Vött 2017; Sorensen 2010). In recent times, several tsunamis worldwide have entailed tremendous damage to coastal communities and infrastructure along with lots of fatalities (e.g., Richmond et al. 2012; Chagué-Goff et al. 2012). In the Mediterranean region, palaeotsunami research has revealed considerable impact of past events (e.g., De Martini et al. 2021; Finkler et al. 2018; Hadler et al. 2015a; Röbke et al. 2015; Vött et al. 2009a). In addition to sediment archives, historical sources provide a reliable indication of the great impact a tsunami can have on coast and society. For the 365 AD tsunami, an event with a large impact on the Mediterranean region, Ammianus Marcellinus described the eyewitness report from Methone, western Peloponnese:

> "For the huge masses of water flowed back when least expected, and now overwhelmed and killed many thousands of people; and when the fury of the waters subsided, some ships were seen to have been destroyed by the rapid whirlpools created by the retreating waters, and the dead bodies of the shipwrecked floated face up or down." (translated by Guidoboni et al. 1994).

An important step to reduce tsunami hazard is to fully understand the processes and related impacts. To this day, the prediction of tsunamis and their impacts on the coast remains a difficult task. Therefore, research is required to reduce the risk to the coastal population. In this context, the study of palaeotsunamis in both historical and sedimentary archives is an important aspect. This data can be used to set up and validate numerical models, which then can help to evaluate potential tsunami hazards on specific coastal areas (Röbke and Vött

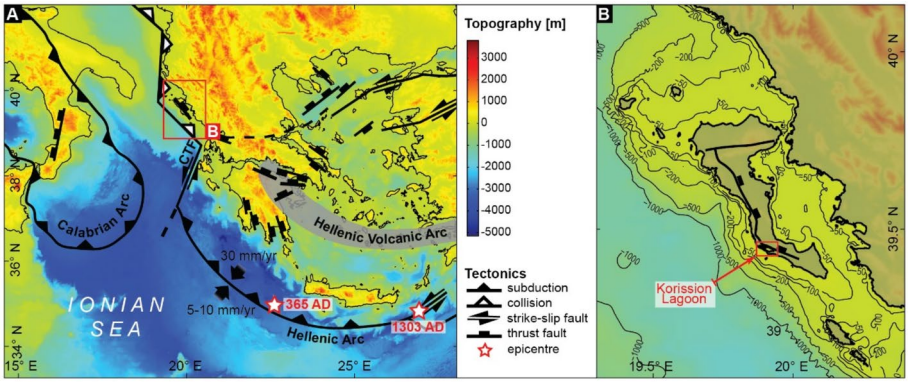

Fig. 1 Overview of the bathymetry, topography, and the tectonic setting of the Ionian Sea (**A**) and Corfu Island (**B**). The epicentres of the 365 AD and the 1303 AD earthquakes according to Lorito et al. (2008) and Hamouda (2006), respectively, are marked with stars

2017). In this context, the objectives of this study are (i) to analyse the local geomorphological inventory and to study sedimentary records in search of potential tsunami signatures, (ii) to reconstruct known tsunamigenic earthquakes, set up a hydrodynamic model for historical tsunamigenic earthquakes with known and previously published seismic parameters, and simulate the propagation of the resulting tsunami waves in the eastern Mediterranean Sea, and (iii) to compare field evidence with results of numerical simulation as a base to better assess the local to regional tsunami hazard. This study focuses on the Korission Lagoon southwest of Corfu Island where, within the frame of a preliminary study by Fischer et al. (2016a), evidence of high-energy impacts was already detected and characterized in form of the sedimentary record of washover deposits. Here, we present additional sedimentological data, radiocarbon ages, and combine field evidence with a hydrodynamic modelling approach for a detailed reconstruction of past tsunami events. The lagoonal setting of the Korission Lagoon, exposed to the open Ionian Sea, as well as the absence of wave action within the lagoon promises ideal requirements for the preservation of potential high-energy deposits and, therefore, the application of our multi-methodological approach.

2 Corfu Island and the Ionian Sea: regional setting, earthquake and tsunami events

2.1 Corfu Island and the Korission Lagoon

Corfu Island is located in the northern Ionian Sea close to the Strait of Otranto marking the transition into the Adriatic Sea (Fig. 1). The island lies within an area of exceptional tectonic stress and has been subject to repeated phases of subsidence and uplift throughout the Holocene, mostly combined with tilting effects (Evelpidou et al. 2014; Finkler et al. 2018, 2019; Mastronuzzi et al. 2014; Papadopoulos and Fokaefs 2005; Pirazzoli et al. 1994).

The Korission Lagoon is located on the southwestern part of the island and extends in a NW–SE orientation parallel to the present-day coastline. On its landward side, the Pleistocene marine sandstones are covered by Holocene aeolian sediments (Darlas et al. 2006; IGME, 1970; Sordinas 1969). The southeastern seaward side of the lagoon consists of uplifted Plio-Pleistocene formations and modern dunes with a maximum height of 15 m whereas the western beach barrier is made out of recent dunes with a height of up to 2 m (Alexopoulos et al. 2007). The Korission Lagoon itself has a maximum depth of 3 m. Towards the west and southwest, it is facing a steep and narrow continental shelf and is, therefore, directly exposed to the open Ionian Sea and to extreme wave events originating from the Hellenic Arc (Fig. 1). Washover fans attached to the recent dunes on the lagoonal side are a geomorphological feature typical of these events (Fig. 2). Fischer et al. (2016a) already reported on sedimentary traces of several high-energy impacts found in sedimentary record of a washover fan on the seaward side of the lagoon.

2.2 The 365 AD earthquake and tsunami

The epicentre of the earthquake that occurred on the 21st of July in 365 AD was located at the reverse fault slip southwest of Crete Island in the Hellenic Arc (Flouri et al. 2013; Shaw et al. 2008; Stiros 2001). The earthquake with an estimated magnitude of $M_W \approx 8.5$

Fig. 2 Overview of the Korission Lagoon **A** showing geological conditions (IGME, 1970) and the location of coring sites and Electrical Resistivity Tomography (ERT) transects (**B** and **C**). Washover fans represent geomorphological features typical of extreme wave impacts (Map: ©Microsoft, 2024)

triggered a tsunami wave travelling through the Mediterranean Sea leaving imprints at many shorelines (e.g., Lorito et al. 2008; Vött et al. 2009a, b; Stiros 2010; Flouri et al. 2013) including Corfu Island (Finkler et al. 2017, 2019). Both, the earthquake and the tsunami are documented in several historical sources (Guidoboni et al. 1994; Vött and May 2009).

Even though the accuracy and the reliability of historical sources must generally be considered carefully (Stiros and Drakos 2006; Hadler et al. 2012), there are plenty of geomorphological and sedimentary traces dated to this time which suggest that the 365 AD event actually occurred. The uplift of western Crete by up to 9 m is supposed to be associated with the 365 AD event (e.g., Ott et al. 2021; Pirazzoli et al. 1982). A controversy exists, however, if the total uplift is a result of a single event (Lorito et al. 2008; Shaw et al. 2008; Stiros 2010) or of several events (Guidoboni et al. 1994). Moreover, historical sources point to a collapse of important structures on Crete Island and the Mediterranean coastline which can be dated to 365 AD (Guidoboni et al. 1994; Ott et al. 2021; Stiros and Drakos 2006). Finally, multi-faceted tsunami deposits were found along the Mediterranean coastline between the islands of Corfu and Crete which are considered to be accumulated by the 365 AD event (e.g., Finkler et al. 2017, 2019; May et al. 2012a; Ott et al. 2021; Werner et al. 2018).

Based on geomorphological observations, traces of radiocarbon dated crust movements and fault parameters that reflect the subduction dynamics in the Hellenic Arc, different seismic scenarios were reconstructed for the 365 AD earthquake (Lorito et al. 2008; Shaw et al. 2008; Papadimitriou and Karakostas 2008; Stiros 2010; Flouri et al. 2013; Table 1).

Table 1 Seismic scenarios and earthquake parameters used in this study to generate initial wave conditions

Tsunami event	References	Strike [deg]	Width [km]	Length [km]	Depth [km]	Dip [deg]	Rake [deg]	Slip [m]	Magnitude [Mw]
365 AD	Lorito et al. (2008)	314	86	130	5	35	90	17.5	8.4
	Shaw et al. (2008)	315	80*	100	45	30	90*	20	8.5
	Papadimitriou and Karakostas (2008)	315	80	160	50	35	90	8.9*	8.3
	Stiros (2010)	292.5	100	105	70	40	90*	16	8.5
1303 AD	Hamouda (2010)	300	35	190	20	45	90	8	8.1
	Yolsal et al. (2007)	115	30	100	20	45	110	8	8

The parameters refer to the geometry of the earthquake-generating fault. Asterisks mark the values determined by Flouri et al. (2013)

2.3 The 1303 AD earthquake and tsunami

On August 8th, 1303 AD, another severe earthquake occurred in the eastern Mediterranean that is documented by multiple historical documents in different languages, mainly Arab, Greek, or Latin. There are, however, uncertainties about the exact location of the epicentre of the earthquake. While a few sources located the epicentre in Egypt, Syria, or near Rhodes, Guidoboni and Comastri (1997) evaluated historical sources and were able to reconstruct that many buildings of Crete were destroyed by the effects of the earthquake. This makes it most likely that the earthquake occurred on the Hellenic Arc near Crete with the epicentre in the southeastern part of the island along a thrust fault. Most sources date the event to the early fourteenth century AD (Guidoboni and Comastri 1997; Hamouda 2006, 2010; Yolsal et al. 2007).

The earthquake with a reported maximum magnitude of $M_W \approx 8.1$ is known to have triggered a tsunami wave. The effects of the tsunami are similar to the ones reported for the 365 AD event with the adjacent coastlines being affected by the extreme wave. Sediment traces were found at the coasts of Greece, Israel, and Egypt, and demonstrate the extent of the triggered tsunami wave (Vött et al. 2006; Hamouda 2006; Papadopoulos et al. 2007; Scheffers et al. 2008; Ntageretzis et al. 2015a, 2015b).

Seismic scenarios for the 1303 AD earthquake were reconstructed using existing studies on inundation and tsunami wave height as well as recent seismic data (Hamouda 2006; Yolsal et al. 2007).

3 Methods

We used a multi-methodological approach combining field work and laboratory analysis with numerical simulations to reconstruct the sedimentary environments of the Korission Lagoon and their changes in space and time.

3.1 Field and laboratory methods

Electrical Resistivity Tomography (ERT) measurements using a Syscal R1 + Switch 48 device (Iris Instruments) and a Wenner-Schlumberger array were carried out to collect

information on the subsurface structure (e.g., Jamaluddin and Umar 2018). Least-square inversion was applied in the Res2Dinv software to process the data (Loke and Barker 1996). Additionally, Direct Push Electrical Conductivity measurements (DP EC) were conducted at Linaria using the Geoprobe SC520 probe with four electrodes in a linear Wenner arrangement with a vertical resolution of <2 cm (Harrington and Hendry 2006). Sediment cores were retrieved by means of a handheld coring device (type Copra Pro, Atlas Copco) with open auger heads and a Nordmeyer Drill Rig type RS0/2.3 with a closed auger system with core diameters of 63 mm and inlying plastic lines of 50 mm, respectively (Fischer et al. 2016b). Half open sediment cores were described and sampled in the field, whereas closed liner cores underwent high-resolution measurements in the laboratory. The position and elevation of ERT transects, DP EC, and coring sites were measured with a Topcon HiPer V Differential Global Positioning System (DGPS) with a precision of 1–2 cm.

In the laboratory, geochemical, mineralogical and foraminiferal proxies were investigated. The grain size distribution was determined using the Köhn method based on subsamples of 15 g (DIN ISO 11277 2020; Köhn 1929). Element concentrations were determined by X-ray fluorescence (XRF) in 2 cm intervals using a portable energy-dispersive analyser (Thermo Niton XL3t 900S GOLDD) in the mode SOIL (e.g., Brouwer 2003; Kalnicky and Singhvi 2001). In order to exclude effects of grain size variations, pore water, or porosity, we use log ratios for our data interpretation (LOG Ca/Fe, LOG Sr/Rb, LOG Zr/Rb, e.g., Profe et al. 2016). Magnetic susceptibility (MS) was measured with a Bartington Instrument and a MS2K surface sensor, and sediment colour with a spectrophotometer (type Konica Minolta CM-600 d), both with a resolution of 1 cm (Dearing 1999; Liu et al. 2012; Viscarra Rossel et al. 2006).

The foraminiferal signature of LIN 1A was studied using 15 ml of sediment extracted from selected sediment samples and sieved into fractions of >400 µm, <400–200 µm and <200–125 µm. For a semi-quantitative analyses, at least 1.6 ml of the material was assessed and foraminifera specimens were identified to group or species level after Loeblich and Tappan (1988) and Murray (1991, 2006) using a stereo microscope (Nikon SMZ 745T). The number of specimens in each sample was extrapolated to 15 ml to ensure comparability.

Plant remains, charcoal, and marine shells were extracted from sediment cores LIN 1A, KOR 19 and KOR 20A for radiocarbon dating. Samples were dated at the Klaus-Tschira Laboratory, Curt-Engelhorn-Centre Archaeometry gGmbH Mannheim, Germany (MAMS), and calibrated using the software Calib 8.2 with the IntCal20 and Marine20 calibration curve (Reimer et al. 2020; Heaton et al. 2020). For core KOR 19, sandwich-dating was accomplished to determine a *terminus ante quem* (before) and a *terminus post quem* (after) for the event. By this approach, reworking effects usually associated with samples from within the high-energy layers can be avoided, where enough sample material is available in under- and overlying stratigraphic units (Vött et al. 2009a, 2011a).

The interpretation of all field and laboratory data was performed in consideration of the results of each individual method, e.g. the results of the ERT measurements were interpreted against the background of the stratigraphic record.

3.2 Numerical simulation

A numerical model based on the Delft3D Flexible Mesh modelling suite (Deltares 2024) was set up to investigate tsunami wave dynamics and associated morphodynamics. Given

the tele-tsunami character of the 365 AD and 1303 AD tsunamis, the model domain covers the entire eastern part of the Mediterranean Sea to simulate a proper wave propagation in the model. We simulated the 365 AD and the 1303 AD tsunamis using different published seismic scenarios. Subsequently, simulation results were compared to field evidence of tsunami impact in order to find the best fit seismic scenario for each event. Different initial wave conditions were used based on the focal mechanisms of each seismic scenario, whereas the model setup was the same for each simulation (Fig. 3). Using the Delft Dashboard software (Van Ormondt et al. 2020), we obtained the bathymetry (GEBCO19, GEBCO 2019), the topography (SRTM, Jarvis et al. 2008) and the initial grid. Additionally, high-resolution digital elevation data (DEM) from the Municipality of Corfu (2017) was used. The final all-in-one computational mesh consists of 894,120 nodes with three refinement steps and a maximum resolution of 610 m by 640 m in the area of the earthquake epicentres, and with seven refinement steps and a maximum resolution of 75 m by 80 m for the Korission Lagoon. The mesh cells are rectangular, and triangular cells are used to connect cells with different resolution.

For the numerical simulation of the 365 AD tsunami, we used the seismic scenarios published by Lorito et al. (2008), Shaw et al. (2008), Papadimitriou and Karakostas (2008), and Stiros (2010) with the values of the focal mechanisms modified by Flouri et al. (2013, Table 1) to create initial wave conditions (Fig. 4). Based on the results of the first runs, the scenarios of Lorito et al. (2008) and Shaw et al. (2008) appeared most appropriate and were chosen for further model calibration (please refer to Supplementary Material for further detail). These scenarios were also chosen by other authors (e.g., Bahrouni et al. 2024, Tunisia).

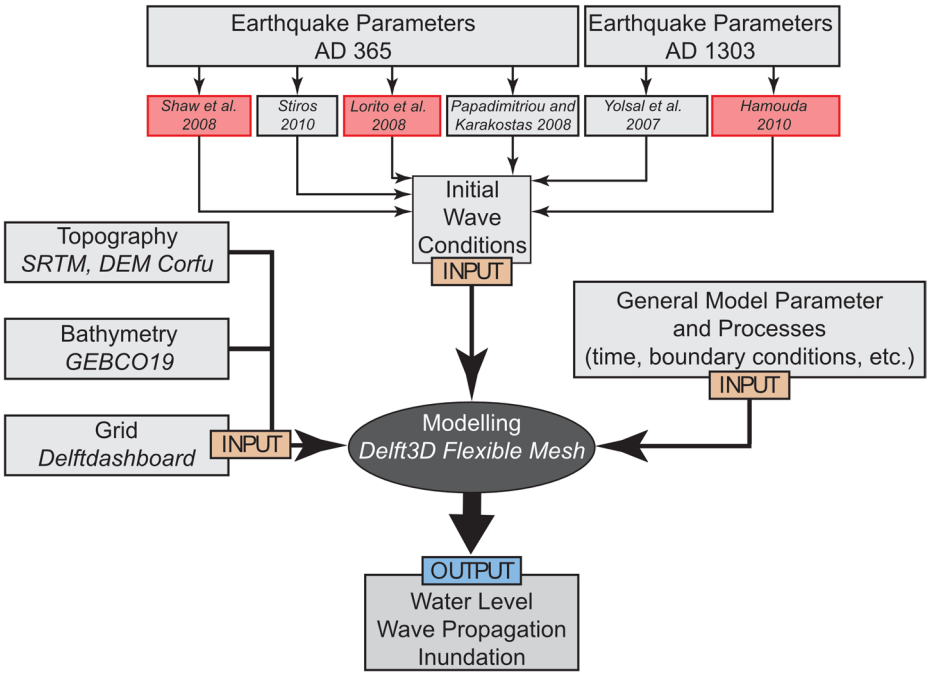

Fig. 3 Model setup used for the simulation of different scenarios for the tsunami events that occurred in 365 AD and 1303 AD in the Mediterranean Sea. The scenarios discussed in this paper are marked in red. Please refer to Supplementary Material for additional scenarios

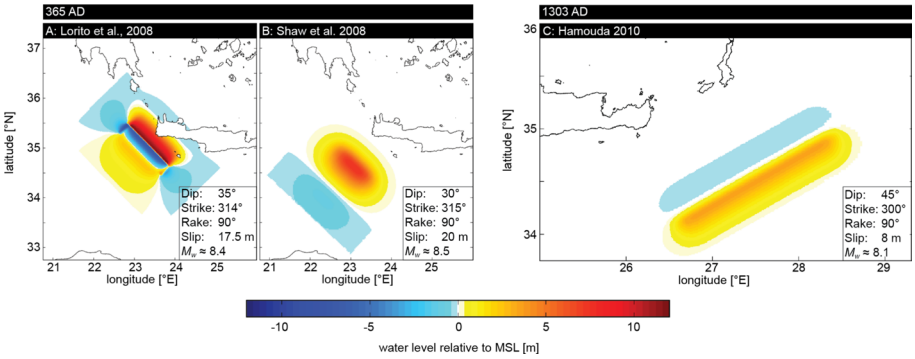

Fig. 4 Initial wave conditions of the 365 AD (**A**, **B**) and 1303 AD (**C**) tsunami calculated based on the seismic scenarios published by Lorito et al. (2008), Shaw et al. (2008), and Hamouda (2010)

For the 1303 AD tsunami, the seismic scenarios by Hamouda (2010) and Yolsal et al. (2007) were used (Table 1, Fig. 4). The tsunami propagation and inundation is computed by the D-Flow Flexible Mesh module of the Delft3D Flexible Mesh suite (version: 3.0.0.2708), which solves the non-linear shallow water equations derived from the three dimensional Navier–Stokes equations for incompressible free surface flow (Deltares 2024). For tsunami simulation, the horizontal and temporal scales are more important compared to the vertical scale. Additionally, vertically stable conditions can be considered for the sea water density which allows the usage of the two-dimensional, depth-averaged model (Röbke et al. 2021).

We conducted a sensitivity analysis for the model calibration of the 365 AD earthquake and tsunami using different parameters affecting the sediment transport (e.g., adaptation of Manning's roughness coefficient n for different bottom roughness, sediment fraction and transport formula, topography and bathymetry, Runs 1–7 for all four seismic scenarios and 9–11 for the (adapted) scenarios by Lorito et al. (2008), and Shaw et al. (2008), partially shown in the Supplementary Material) and compared the results with the sedimentary data obtained in the field (see sensitivity analysis in Supplementary Material). Since we assume the beach ridge as the main source of sediment relocated during a high-energy event, we defined one sediment fraction based on the in-situ conditions: Fine sand with an average grain size of 0.14 mm and an initial sediment thickness of 5 m for the setup of the morphodynamic model. We used a uniform Mannings friction coefficient n of 0.02 s $m^{-1/3}$ and the sediment transport was simulated using the transport formula by van Rijn (1993).

For the Korission Lagoon, both the palaeodepth of the lagoon and the palaeoheight of the beach ridge were adapted based on data from core KOR 19 to take possible tectonic influences into account and to test the effects of a higher or lower sea level. Based on the recent setting, we chose a depth of 3 m for the first run. Additionally, we tested the effects of potential tectonic movements after the 365 AD tsunami event. For subsidence after the event, we chose a shallower bottom level of 0.5 m and, to test tectonic stability, a deeper bottom level of 4 m which corresponds with the depth of the deposits found in sediment core KOR 19. Additionally, we considered different heights of the beach ridge (0.5 m, 1 m, and recent height of around 2 m) and, based on the stratigraphy and dating of KOR 19, removed the washover fans in the lagoon. For the earthquake parameters themselves, we tested the impact of the slip rate and dip angle of the seismic scenarios. For the sensitivity analyses of the 1303 AD event, we increased the slip rate by 5 m, the dip angle by 5°, and tested the

effects of the waves on the different lagoonal settings as described for the 365 AD event as well as a combination of multiple tsunamigenic sources (not shown).

We ran a total of 10 simulations for the 365 AD tsunami using the (modified) seismic scenario of Lorito et al. (2008) and 7 simulations using the scenario by Shaw et al. (2008, see also Table 2 and Supplementary Material) and 7 simulation the seismic scenarios of the 1303 AD tsunami (Hamouda 2010; Yolsal et al. 2007, not shown). Based on the simulation results, additional observation points were set to extract point data for specific locations and compare them with the field evidence of tsunami landfall.

4 Results

4.1 ERT transects

Two ERT transects were measured along the coastline of the Korission Lagoon to investigate the subsurface (Figs. 2, 5): one in the southeast of the lagoon at Linaria, one on the washover fan in the southwest, and one on the opposite, landward lagoonal shore.

The ERT depth section for Linaria (LIN ERT 1, Fig. 5A) shows lower resistivity values at the top and higher values towards the bottom with a sharp transition. Compared to that, the resistivity values of the ERT transect KOR ERT 68 measured perpendicular to the spit on the washover fan at the second site are significantly lower. There is, however, a zone of comparatively higher values at a depth of 1–3 m (Fig. 5B).

4.2 Stratigraphic data from sediment cores

Four sediment cores were retrieved from the Korission Lagoon (see Fig. 2 for coring sites). First stratigraphic data presented by Fischer et al. (2016a) was analysed in detail and classified into sedimentary units A to E. Cores KOR III, IV and V in Fischer et al. (2016a)

Table 2 Overview of the 17 model setups used as base for numerical simulation of tsunami landfall scenarios discussed in this study

Please note the differences in the dimension of geomorphological features (depth of lagoon and height of beach ridge) and adapted earthquake parameters listed for the model setups. All adaptations of model setups differing from the original data published by Lorito et al. (2008) and Shaw et al. (2008) are written in italics

Scenario	Depth of the Korission Lagoon (D_L) [m]	Height of the Beach Ridge (H_{BR}) [m]	Slip [m]	Dip [deg]
Run08	DEM	DEM	17.5	35
Run09L	*− 0.5*	*0.5*	17.5	35
Run09S			20	30
Run10L	*− 4*	*0.5*	17.5	35
Run10S			20	30
Run11L	*− 0.5*	DEM	17.5	35
Run11S			20	30
Run12L	*− 4*	DEM	17.5	35
Run12S			20	30
Run13L	*− 0.5*	*1*	17.5	35
Run14L	*− 4*	*1*	17.5	35
Run15L	*− 4*	DEM	*20*	35
Run15S			*22.5*	30
Run16L	*− 4*	DEM	*22.5*	35
Run16S			*25*	30
Run17L	*− 4*	DEM	*20*	*40*
Run18L	*− 4*	DEM	*22.5*	*40*

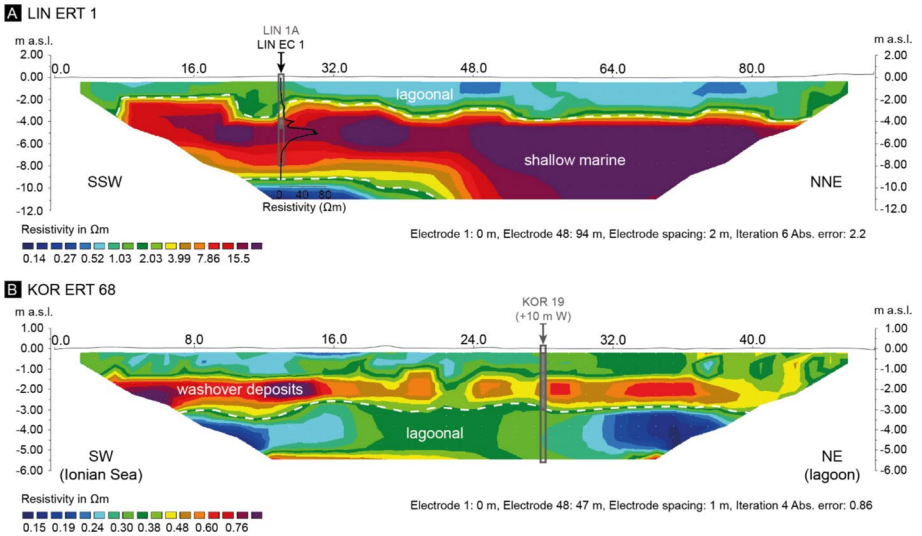

Fig. 5 Depth sections of ERT transects LIN ERT 1 (**A**), and KOR ERT 68 (**B**). Overall low resistivity values are related to saltwater influence. Please note that we used different scales for the transects in order to optimize visibility of the local differences for each transect

correspond to cores KOR 19, 21, and 20 in this paper, respectively. Sediment core KOR 19 was drilled on the distal part of a washover fan at the western shore of the lagoon at an elevation of 0.11 m above sea level with a total depth of 6 m (5.89 m below sea level). Basal clayey silt is followed by alternating sequences of fine to medium sand and intercalated fine-grained sediments (Fig. 6). Sediment cores KOR 20A and 21A, drilled at 0.13 and 0.08 m above sea level at the landward lagoonal shore opposite to the washover fans, reveal partly weathered fine sand at the base, covered by sands intersecting clayey silt (please refer to Fischer et al. (2016a), for a more detailed description of the sedimentary record of both sediment cores). Sediment core LIN 1A was retrieved from the coastline at the southeastern part of the lagoon at an elevation of 0.12 m above sea level with a total depth of 8 m (7.88 m below sea level). It consists of fine to medium sand at its base (to 5.25 m b.s.) with layers of sand, clayey silt, and silty clay in its upper part (Fig. 7).

4.3 Direct push sensing

DP EC measurements were conducted to a depth of 9.26 m b.s. at coring site LIN 1A (Fig. 2). The log shows high conductivity values at the base and the top of the sequence and low values in the middle (Fig. 7). The conversion into resistivity values enables to better detect three peaks of higher values at 2.73 m b.s., 3.98 m b.s., and 5.09 m b.s. Following each peak, the values decrease at a slow rate for 10–50 cm followed by a sharp transition and rapidly decreasing values.

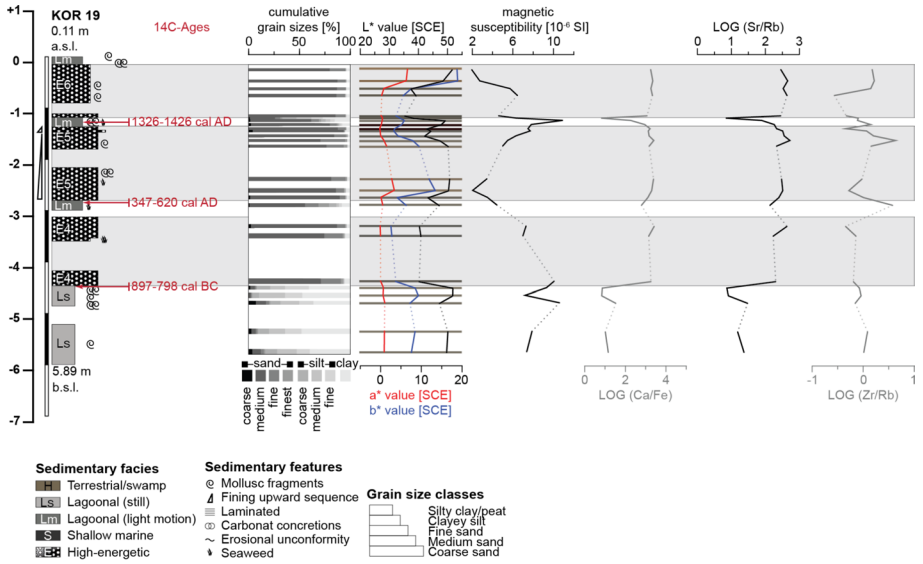

Fig. 6 Stratigraphic log of sediment core KOR 19 drilled on top of a washover fan at the western shore of the Korission Lagoon including calibrated radiocarbon ages, grain size distribution, colour, magnetic susceptibility (MS), and selected geochemical proxies. Grey boxes indicate high-energy events; dotted lines are used to connect measured sections

4.4 Microfaunal analyses

Detailed microfaunal analysis was carried out for sediment core LIN 1A. Microfaunal studies for sediment cores KOR 19 and 20 were already presented by Fischer et al. (2016a). Based on Murray (1991; 2006), detected foraminifera were grouped according to their habitats and associated sedimentary environments, namely into lagoonal to shallow marine, marine, cold marine, epifaunal, and planktonic; Ostracoda were grouped into brackish or marine environments. Total abundances and origin obtained from the microfaunal analyses helps to classify sedimentary environments and to define the origin of the sediment. Our results show highest abundances and diversities in sandy layers compared to layers with clayey silt (Fig. 8). The latter revealed more brackish and lagoonal to shallow marine species (e.g., *Ammonia beccarii*, *Haynesina* spp.) whereas in sand layers marine and cold marine species from the shelf to bathyal area occur (e.g., *Cassidulina* sp., *Lenticulina* sp., Fig. 8). Microfaunal data obtained for cores KOR 19, 20A and 21A show the same abundances for the different sedimentary environments: In layers dominated by clayey silt, only autochthonous, brackish to lagoonal species such as *Ammonia beccarii* were observed, whereas in sandy units, the diversity increases and allochthonous species like *Globigerina* sp. and *Elphidium crispum* were found (Fischer et al. 2016a).

4.5 Multi-proxy analyses

Results of multi-proxy analyses for KOR 19 show medium to low values of all parameters for the lower section of the sediment core (Fig. 6). With the appearance of the first sand layer, the values change significantly: LOG Ca/Fe and LOG Sr/Rb ratios increase

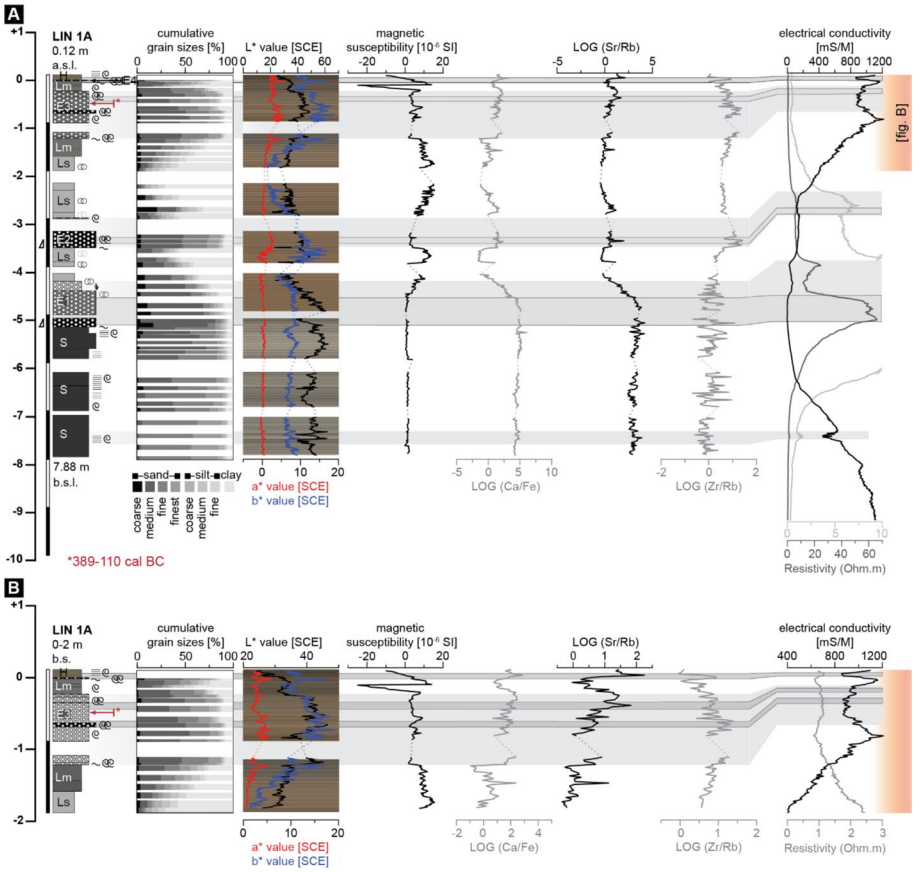

Fig. 7 Stratigraphic log of sediment core LIN 1A drilled at the southeastern shore of the Korission Lagoon including calibrated radiocarbon ages, grain size distribution, colour, magnetic susceptibility (MS), and selected geochemical proxies for the whole sediment core (**A**) and for the upper four meters (**B**). Dark grey boxes indicate high-energy events, light grey boxes indicate potential further events and event-related deposits. Note that dotted lines are used to connect measured sections and different scales for resistivity were used in A to resolve coarse-grained layers. See Fig. 6 for legend

and remain at highest observed levels and only decrease in the thin layers of finer grained material. Contrary to that, the MS values decrease throughout the core, and a peak can be observed in the finer grained layer at 1.20 m b.s.

The multi-proxy data obtained for sediment core LIN 1A show little variation of the parameters for the lower core section, apart from the LOG Zr/Rb ratio (Fig. 7). Towards the top, LOG Ca/Fe and LOG Sr/Rb ratios decrease while the MS values increase. In the upper meter, this tendency is reversed, with a minimum in MS at 0.23 m b.s. and maxima at 0.12–0.08 m b.s. in the log ratios. Additionally, there are smaller but clearly visible sharp transitions at 3.61 and at 1.33 m b.s. regarding all parameters (decrease in MS, increase in the log ratios, Fig. 7).

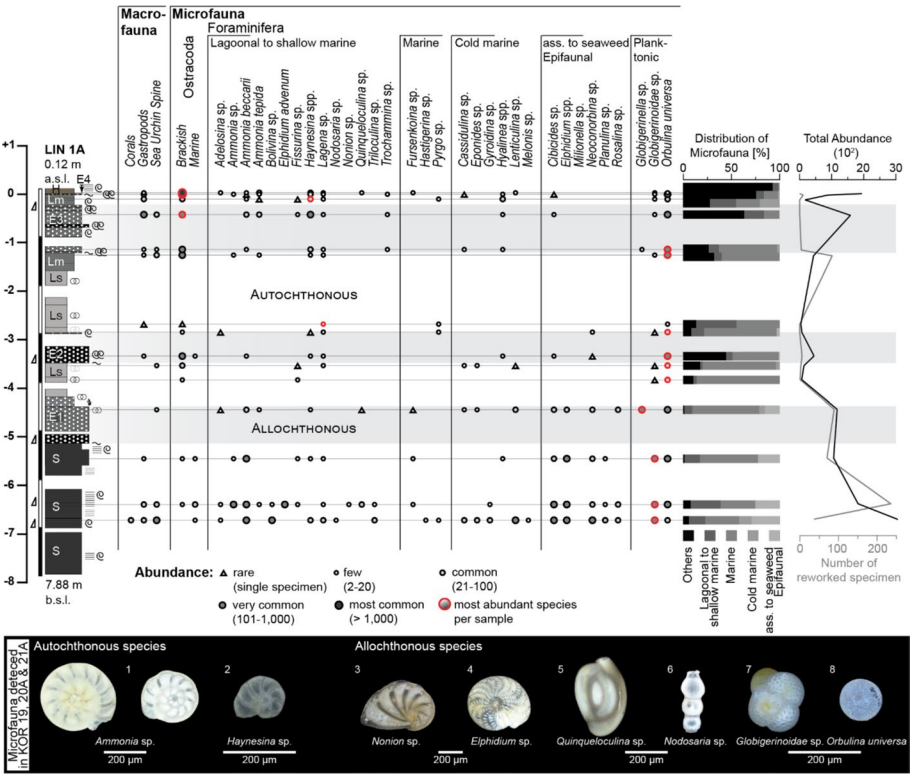

Fig. 8 Semi-quantitative overview of microfauna remains detected in sediment samples from sediment core LIN 1A (top) and selected species found in sediment cores KOR 19, KOR 20A, and KOR 21A (see Fischer et al. 2016a for details). The analyses allow a classification into autochthonous and allochthonous origin. See Fig. 6 for legend of the stratigraphic record and Supplementary Material for absolute numbers of detected specimen

4.6 Classification of sedimentary units

Based on the sedimentary characteristics and the results of laboratory analyses, we found different sedimentary units (Table 3). The basal unit S consists of consolidated material in sediment cores KOR 20A and 21A, and of laminated unconsolidated sands in sediment core LIN 1A. Unit L which marks the basal sediment in sediment core KOR 19 was found in all sediment cores and is characterised by silt to clayey silt. This unit dominates the upper half of sediment core LIN 1A and parts of core KOR 19, still, it is repeatedly interrupted by sand layers of unit E. In the upper sections of sediment cores KOR 20A, KOR 21A, and LIN 1A, clayey silt with root fragments and organic compounds (humus) was observed (unit H).

4.7 Radiocarbon dating

Five samples were dated using the ^{14}C-dating approach (Table 4). For core LIN 1A, an age of 389–110 cal BC was found at a depth of 0.60 m b.s. (0.48 m b.s.l.), and for core KOR 20A radiocarbon dating yielded an age of 1283–1388 cal AD at a depth of 0.69 m b.s.

Table 3 Stratigraphic units found in sediment cores LIN 1A, KOR 19, KOR 20A, and KOR 21A drilled along the shores of the Korission Lagoon

Sedimentary unit	Sediment core and depth [m b.s.l.]	Grain size	Colour	Microfauna	Sedimentary characteristics	Facies interpretation
S	LIN 1A: 8.00–5.25	Fine to medium sand, partly silty	Grey	High abundance of shallow and cold [?] marine species and species from epifaunal habitats reworked species most abundant: *Globigerinoidae* sp.	Rich in $CaCO_3$ partly laminated	Shallow marine
	KOR 20A:1.43–0.85 KOR 21A:1.43–1.02	Fine sand	(Rusty) grey	–	Marbled mollusc fragements Fe- and Mn-concretions	
E	LIN 1A: 5.25–4.303.60–2.96 1.33–0.34 0.13–0.11 KOR 19: 4.47–3.13 2.80–1.37 1.18–0.15 KOR 20A: 0.85–0.78 0.60–0.39 KOR 21A: 1.02–0.48 0.38–0.29	Medium sand, partly silty	White, beige, grey	High abundance of marine species mixed species from different marine environments allochthonous character (**ex situ**), washed in lagoonal sedimentary environment	Rich in $CaCO_3$ high values of DP resistivity peaks in LOG Sr/Rb and LOG Zr/Rb fining upward mollusc fragments basal erosional unconformities (LIN 1A, KOR 20A)	High-energy deposits
L	LIN 1A: 4.30–3.60 2.96–1.33 0.34–0.13 KOR 19: 6.00–4.47 3.00–2.80 1.37–1.18 0.15–0.13 KOR 20A: 0.78–0.60 KOR 21A: 0.48–0.38	Clayey silt	Grey, partly rusty, beige and black	Low abundance and diversity of species most abundant: *Haynesina* spp., *Lagena* sp., and *Orbulina universa*	Increase in magnetic susceptibility	Lagoonal
H	LIN 1A: 0.11–0.00 KOR 20A: 0.60–0.00 KOR 21A: 0.29–0.00	Clayey silt	Grey to brown	–	Party laminated enriched organic matter	Topsoil/colluvial

(0.56 m b.s.l.). Three samples of core KOR 19 from layers of finer sediments yielded ages of 897–789 cal BC at a depth of 4.48 m b.s. (4.37 m b.s.l.), 347–620 cal AD at 2.85 m b.s. (2.74 m b.s.l.), and 1326–1426 cal AD at 1.27 m b.s. (1.16 m b.s.l.).

4.8 Numerical simulation

For the 365 AD tsunami, maximum wave heights were simulated for the western part of Crete, the southern and southeastern coasts of the Peloponnese, and in a southwestern direction towards the African coast, especially towards Libya and Tunesia. Since the scenario based on the fault parameters by Lorito et al. (2008) generally suggests a closer agreement between the simulated morphodynamics and field traces compared to the scenario by Shaw et al. (2008, Fig. 9A, B) further analyses are restricted to the scenario based on Lorito et al. (2008; for the analysis of Shaw et al. (2008), see Supplementary Material).

For the 365 AD scenarios and its effects on the Korission Lagoon, we used multiple sensitivity runs (see Sect. 3.2) and obtained the most promising results for Lorito et al. (2008) with a deeper bottom level of the lagoon and the recent height of the beach ridge. We tested this setting with alterations of the slip rate of the earthquake. These best-fit numerical simulation scenarios show that the lagoon is inundated from southwest to west to variable extents. In contrast, there is no water inflow into the lagoon from a southern direction even though the maximum wave heights can be observed in this area (Fig. 10). While the water level in the lagoon remains lower in the reference run (Fig. 10A_1), it is higher in the northwest and southeast in the other runs, with highest values in Run16L (Fig. 10A_3). A similar trend can be observed in the velocity magnitude, where the lowest values in the lagoon were found in the reference run (Fig. 10B_1) and the highest in Run16L (Fig. 10B_3). Besides, the map view of the velocity magnitude shows areas of significantly higher velocities at four locations of the beach ridge which become more distinct with the adaptation of the slip rate

Table 4 Radiocarbon ages of samples collected from sediment cores drilled along the shores of the Korission Lagoon

Sample ID	Depth (m b.s.)	Depth (m b.s.l.)	Sample material	Lab. no. (MAMS)	^{14}C Age (yr BP)	2σ Age (cal BC/AD)	1σ Age (cal BC/AD)
LIN 1A/10+M	0.60	0.48	Shell, *crobicularia plana*	43659	2679±22	389–110 cal BC*	341–194 cal BC*
KOR 19/7 PR	1.27	1.16	Plant remains, unidentified	45695	544±20	1326; 1426 cal AD	1399–1421 cal AD
KOR 19/16+M	2.85	2.74	Shell, *Cerastoderma glaucum*	45696	2068±23	347–620 cal AD*	422–557 cal AD*
KOR 19/21 PR	4.48	4.37	Plant remains, unidentified	45697	2671±21	897; 789 cal BC	829–805 cal BC
KOR20/10+HK	0.69	0.56	Charcoal	45698	662±19	1283; 1388 cal AD	1290; 1383 cal AD

b.s. below ground surface, b.s.l. below sea level, Lab. No. laboratory number of the Klaus-Tschira Laboratory of the Curt-Engelhorn-Centre Archaeometry gGmbH Mannheim, Germany (MAMS), 1σ/2σ calibrated age ranges; means multiple intersections with calibration curve. Conventional ages are calibrated in Calib 8.2 using the IntCal20 curve (Reimer et al. 2020) or the Marine20 curve with an MRE of 550 years (marked with *, Heaton et al. 2020)

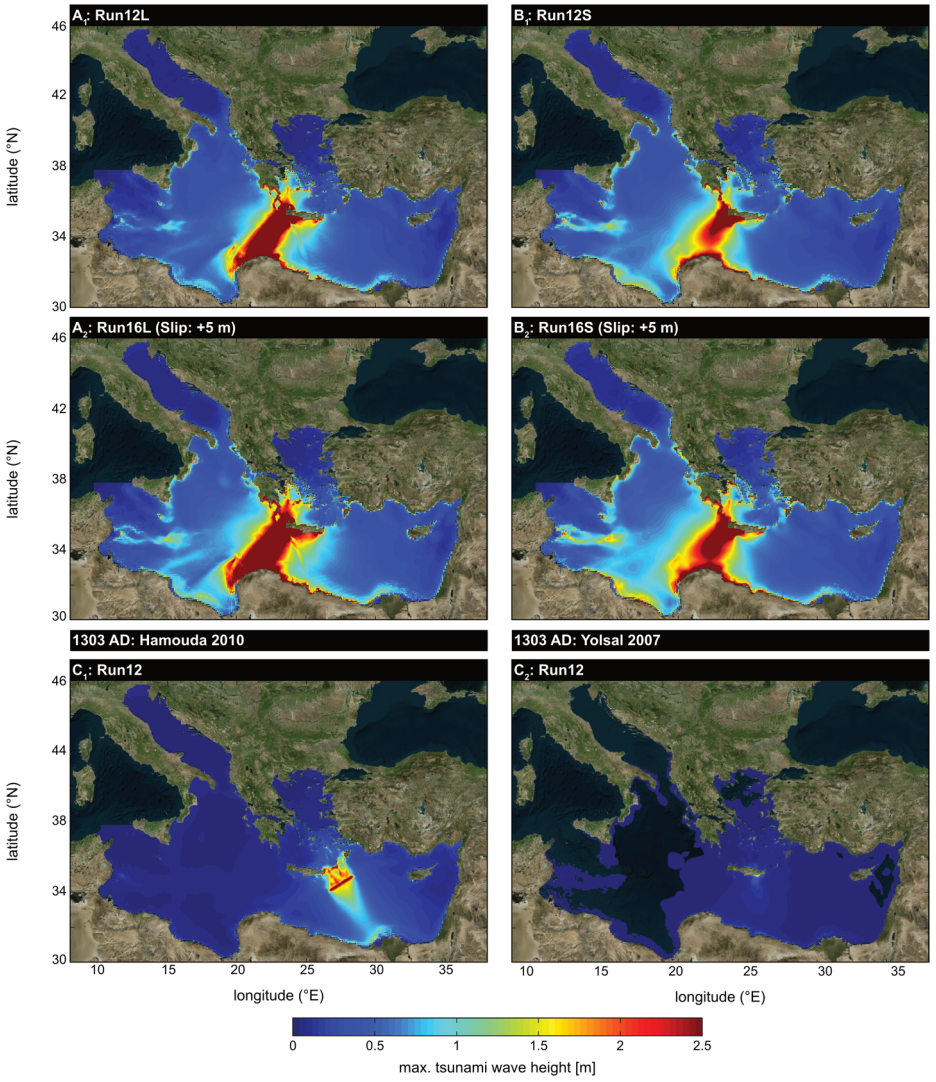

Fig. 9 Maximum tsunami wave heights as simulated for different scenarios of the 365 AD and the 1303 AD tsunamis based on published fault parameters (Lorito et al. 2008, **A**; Shaw et al. 2008, **B**; Hamouda 2010, **C**, see Table 2 for scenario descriptions, Map: ©Microsoft, 2024)

of the earthquake by an additional 5 m (Run16L, Fig. 10B_3, Supplementary Material for further adaptation results).

This pattern is also visible in the maps showing the cumulative erosion and sedimentation (Fig. 10C). In areas of higher velocities, erosion takes place at the beach ridge and sedimentation directly adjacent to the north and south resulting in the formation of washover fans. These fans are smallest in the reference run (Fig. 10C_1) and become larger in size with increasing adaptation of the topography and earthquake parameters. Sedimentation and erosion increase with these adaptations from minimum + 0.76 m (sedimentation) and

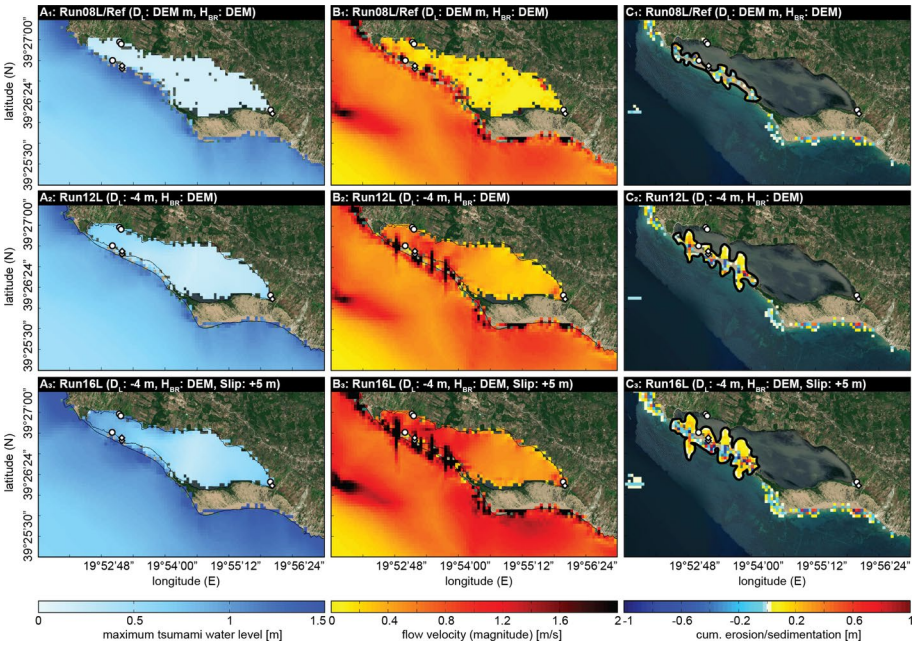

Fig. 10 Numerical simulation scenarios of the tsunami event 365 AD and their effects on the Korission Lagoon. Simulation runs differ with regard to depth of the lagoon (D_L), height of the beach ridge (H_{BR}), and adaptation of the slip rate (see Table 2 for further information). Simulated water level (**A**), flow velocity (**B**), and erosion/sedimentation (**C**) are depicted for different runs based on Lorito et al. (2008, Map: ©Microsoft, 2024)

Table 5 Erosion and sedimentation modelled for three observation points (Obs1 and Obs2 near KOR 19, Obs3 near LIN 1A) based on selected model runs compared with thickness of tsunami deposits observed in sediment cores

Observation Point	Location		Sedimentation and Erosion				
	Latitude (°N)	Longitude (°E)	RunRef	Run12L	Run15L	Run16L	Field traces
Obs1	39.448093	19.886431	0	−1.3	−1.664	−2.065	–
Obs2 (KOR 19)	39.448782	19.886431	0.003	+0.757	+0.843	+0.825	+1.47
Obs3 (LIN 1A)	39.437537	19.933693	0	+0.0007	+0.003	+0.011	+0.02

Please refer to supplementary material for further results

−1.3 m (erosion) in Run12L to maximum +0.83 m (sedimentation) and −2.07 m (erosion) in Run16L (see Table 5). At coring sites LIN 1A and KOR 20A, smaller variations of the sedimentation can be observed (Fig. 10C and Table 5).

In the last step, we increased the dip angle by 5°. This adaptation leads to a considerable growth of the washover fans and to the input of large amounts of sediment into the lagoonal environment (Fig. 11). Wave heights larger than 0.4 m cause an increase in the bottom level by about 1.1 cm at observation point Obs4, close to sites KOR 20A and 21A.

The simulation results based on fault parameters of the 1303 AD event by Hamouda (2010) show that tsunami waves travel from the southeastern part of Crete towards the coast

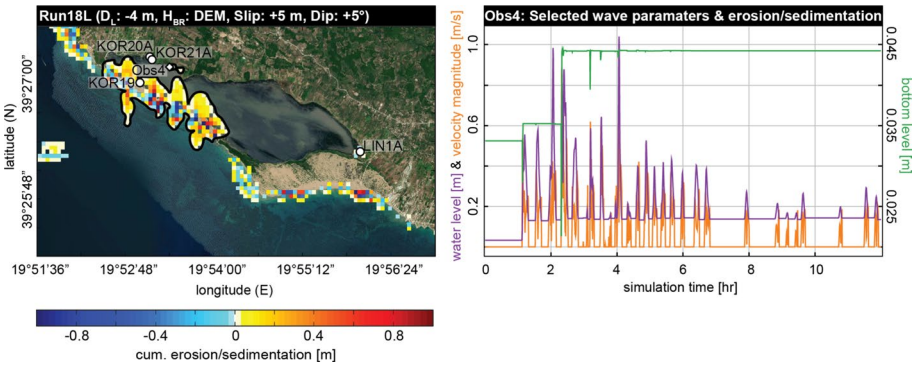

Fig. 11 Numerical simulation of the 365 AD tsunami event with results of the simulation Run18L. Map on the left shows effects of cumulative erosion/sedimentation (left); graphs on the right hand depict water level, flow velocity, and bottom level calculated for observation point Obs4 (location indicated on the map, see Table 2 for further information, Map: ©Microsoft, 2024)

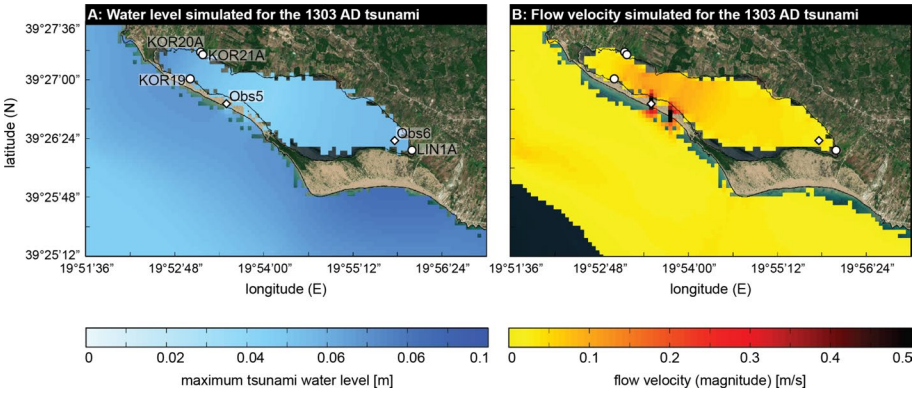

Fig. 12 Maximum tsunami water level (**A**) and flow velocity (**B**) for the 1303 AD tsunami simulated based on seismic settings presented by Hamouda (2010, Map: ©Microsoft, 2024)

of Egypt (Fig. 9C). Even though the tsunami propagates in the entire eastern Mediterranean Sea, the maximum water levels are clearly lower compared to the 365 AD tsunami.

Based on the seismic scenario by Hamouda (2010), we applied the lagoonal setting of Run12L (depth of the lagoon: −4 m, recent height of the beach ridge) for the simulations of the 1303 AD tsunami. The simulation results only show a small increase in the maximum tsunami water level in the lagoon (Fig. 12A). Similar to the 365 AD tsunami event, the flow velocity is highest at two locations on the beach ridge (Fig. 12B). Still, neither erosion nor sedimentation occur in the model and the values of both, water level and flow velocity, are considerably lower than in the 365 AD tsunami scenarios. Besides the scenario by Hamouda (2010), we also simulated the tsunami impact based on the seismic scenario by Yolsal et al. (2007), which, however, does not show any morphodynamic responses in the lagoon.

5 Discussion

5.1 Sedimentary record of the Korission Lagoon

Overall, four stratigraphic units were defined (Table 3). Pre-lagoonal sediments were found at the base of sediment cores KOR 20A, KOR 21A, and LIN 1A. These basal fine-sandy deposits (unit S) reflect shallow marine conditions and are represented by higher resistivity values in the ERT transect LIN ERT 1 (Fig. 5A). At coring site LIN 1A, this is supported by low resistivity values in the DP EC log, low MS values as well as relatively higher LOG Sr/Rb values and highly variable LOG Zr/Rb values reflecting higher flow dynamics. In addition, the microfaunal content shows a high diversity and abundance of the detected species related to shallow marine to marine conditions (Fig. 8, Murray 1991, 2006). This basal sediment seems to result from a time before the closure of the lagoon when the coastline of the Ionian Sea was near the coring sites and a marine influence prevailed.

The basal unit S is overlain by coarse-grained deposits of unit E which is represented by peaks in the resistivity values of the DP EC log at coring site LIN 1A. The basal unit in sediment core KOR 19 consists of lagoonal deposits and is overlain by high-energy deposits of unit E. On top of these high-energy event deposits, lagoonal conditions represented by clayey silt were established (unit L) at all coring sites. This is also shown by lower resistivity values in ERT depth sections of transects LIN ERT 1 and KOR ERT 68 (Fig. 5) and by DP EC log data obtained from coring site LIN 1A. Additionally, a relative decrease of LOG Ca/Fe, LOG Sr/Rb, and LOG Zr/Rb values accompanied by increasing MS values indicate reduced marine influence. This is further supported by a decrease in the total abundance and diversity of microfauna. Lagoonal sediments were found in different thicknesses in all sediment cores and were repeatedly interrupted by event deposits (unit E) in sediment cores LIN 1A and KOR 19. At the top of sediment core LIN 1A and in sediment cores KOR 20A and 21A, lagoonal conditions were not restored after the last high-energy impact, but terrestrial conditions (topsoil/colluvial) were established which still prevail until the present day.

5.2 Origin of high-energy deposits

Sedimentary records taken from the Korission Lagoon show multiple stratigraphic and geomorphological evidence for repeated high-energy events. The allochthonous sandy deposits of unit E intersecting the autochthonous lagoonal deposits of unit L, mark high-energy impacts into the Korission Lagoon. This signature is commonly observed in Mediterranean coastal areas in conjunction with tsunami landfall (Goff et al. 2012; Röbke and Vött 2017; Vött et al. 2011a). The input of coarser-grained sediments of marine origin is also represented in the geochemical proxies: Within unit E, peaks can be observed in LOG Ca/Fe, LOG Sr/Rb, and LOG Zr/Rb values (marine origin) while MS as tracer for terrestrial origin of sediments decreases (Figs. 6, 7, e.g., Goff 2008; Costa et al. 2012; May et al. 2012a, b; Hadler et al. 2015a, b; Chagué-Goff et al. 2016). DP EC data show corresponding peaks in the resistivity values indicating coarser sediments (Fig. 7, Schulmeister et al. 2003). Abrupt changes of the geochemical proxies between high-energy deposits and underlying sediments indicate a rapid change of the sedimentary environment which may be interpreted as a clear sign of such high-energy impacts (e.g., Chagué-Goff 2010). In sediment cores LIN 1A and KOR 20A, this is underlined by clear basal erosional unconformities (e.g., Chagué-

Goff et al. 2011). Additionally, a fining inland of the deposits can be observed: While at coring site KOR 19, more than 1 m of sediment was deposited during each event, event layers become thinner towards inland (> 0.24 m at coring sites KOR 20A and KOR 21A. This fining landward tendency is typical of high-energy deposits and is due to loss of energy with increasing distance from the coastline (Goff et al. 2012; Kortekaas and Dawson 2007) which, in the case of the Korission Lagoon, is at the beach ridge. The microfaunal analysis of sediment cores LIN 1A, KOR 19, and KOR 20A reveal relatively higher abundances and diversities of species within the high-energy deposits. Here, especially marine, cold marine, and epifaunal species were observed while shallow marine and marine species were dominant in the (basal) lagoonal (unit L) and basal shallow marine (unit S) deposits. This documents the input of allochthonous sediments from a different depositional environment as well as event-related mixing of these sediments. The latter is especially true for the lagoonal sediment found in between high-energy deposits at site KOR 19 where the diversity and abundance of microfauna remain high. The washover fans along the western beach barrier as geomorphological forms clearly indicate high-energy impacts and sediment transfer from the open sea into the lagoonal environment (Clemmensen et al. 2014; Fischer et al. 2016a; Gianfreda et al. 2001; Switzer et al. 2006).

Due to the exposition of the Korission Lagoon towards the open Ionian Sea and a relatively steep continental slope, the lagoon is at risk of both storm- and tsunami-related high-energy events. Even though, storms and resulting waves generated by Sirocco phenomenon and Medicanes usually propagate farther north- and southward, respectively, they are known to impact the Ionian Sea (Gaertner et al. 2018; Lionello et al. 2008; Soukissian et al. 2007). Storms from the west wind zone have been observed to hit the Peloponnese and the southern Ionian Islands (Diakakis et al. 2023; Pytharoulis et al. 2000), and Sabatier et al. (2012) suggest that storms may have been stronger and more frequent during specific periods in the past. Thus, storms must generally be taken into account as a cause for the high-energy deposits in the Korission Lagoon.

In general, strong storms in the Mediterranean are much more frequent than strong tsunamis (frequency of dozens per century compared to few per millennium; see Vött et al. 2019). Therefore, the potential storm imprint on the lagoonal environment should be much more frequent and repeated, resulting in a sequence of many sand layers regularly intersecting lagoonal muds. In contrast, tsunamis must be considered as episodic extreme events. The sedimentary signature on the west coast of Corfu consists of few but thick layers of allochthonous sand. This sedimentological observation rather indicates tsunami origins than storm influence. Additionally, tsunami waves have long wave lengths up to 500 km in the open sea and 10 km in coastal areas while the wave lengths of wind generated waves and storms are much shorter which also reduces their inland extent (Kortekaas and Dawson 2007; Röbke and Vött 2017). The washover fans as geomorphological traces of tsunami wave impact (Gianfreda et al. 2001; May et al. 2012a) and the sedimentary evidence in all sediment cores obtained from the coastline of the lagoon reveal that these events must have affected the whole area (see Sect. 5.2). Furthermore, radiocarbon ages indicate that both washover fans at the seaward lagoonal shore and sedimentary traces at the landward shore were possibly caused by same event which is likely identical with the historically known tsunami event in 1303 AD (see Sect. 5.4).

5.3 Chronology of extreme wave impacts—the Korission Lagoon transect

Based on sediment core stratigraphies and radiocarbon ages, it was possible to establish a chronostratigraphy of the lagoonal development and different extreme wave impacts. Pre-lagoonal deposits of unit S found in sediment cores KOR 20A, KOR 21A and LIN 1A mark the oldest sediments found in the environs of the Korission Lagoon. Rapid sea level rise until ~6 ka BP prevented the formation of lagoons and deltas in the Mediterranean. The earliest onset of their formation coincides with the deceleration in sea level rise (e.g., Chabrol et al. 2025; Fouache et al. 2008; Haenssler et al. 2014). For the Korission Lagoon, we conclude that the basal shallow marine deposits are likely of early to mid-Holocene age and document open-bay conditions prior to the formation of the lagoon. These conditions still prevailed when the first high-energy event hit the lagoon (subunit E1, Fig. 7, Table 6). Following high-energy deposits, sediment core LIN 1A reveals an overall change in the depositional environment to low-energy lagoonal mud. This implies that the coastline configuration was significantly changed, most probably as consequence of the extreme wave impact itself. After the establishment of the lagoon, it was repeatedly hit by high-energy events. Due to a lack of datable material, it is not possible to ascribe the first and second event deposits (subunits E1 and E2) to specific events. Still, previous studies have dated multiple high-energy events in the Ionian Sea between the 6th and 2nd millennia BC (Finkler et al. 2017, 2019; Vött et al. 2009a, 2011a, b; Willershäuser et al. 2013, 2015) which have also affected the Korission Lagoon and left traces in the sedimentary record. Further dating approaches are, however, needed to clarify their timing. In contrast, the third high-energy event could be dated to 389–110 cal BC using the radiocarbon dating approach (subunit E3, Fig. 13, Tables 4 and 6). This age represents a *terminus ad quem* for the event and would fit well with a known tsunami occurring in the fourth and third century BC if potential reworking as well as marine reservoir effects are excluded. At that time, Corfu Island was affected by a co-seismic uplift associated to a local earthquake (Finkler et al. 2018; Mastronuzzi et al. 2014). Evidence for younger uplift events are not present at the Korission Lagoon. Here, the oldest radiocarbon age obtained for sediment core KOR 19 documents that the lagoon was already well established before 897–798 cal BC (Fig. 13, Table 4). At the same time, this age is a *terminus post quem* for the first high-energy event (subunit E4, Table 6) documented within the sedimentary stack of local washover fans. On top of these deposits, lagoonal mud accumulated right after event IV and was dated to 347–620 cal AD. This age thus functions as a *terminus ante quem* for event IV (Fig. 13, Table 4). The fact that the age obtained from right underneath the base of event layer IV is much older (897–798 cal BC, see above) might be associated to erosional processes during the inflow of tsunami waters. Event IV, therefore, seems to be associated with the 365 AD earthquake and tsunami event. These findings are in line with findings from other studies along selected coasts of the eastern Mediterranean that yielded geomorphological and geochronological evidence of the landfall of the 365 AD tsunami. Along the Greek and Italian coastline of the Ionian Sea, traces were found along the Gulf of Corfu (Finkler et al. 2017, 2018, 2019), the Lagoon of Lefkada and the Bay of Nikolaos (May et al. 2012a, b; Vött et al. 2008, 2009b), Lake Voulkaria and the Bay of Palairos-Pogonia (Vött et al. 2009a, 2011b), the Gulf of Kyparissia (Willershäuser et al. 2015), the harbour site of Kyllini (Hadler et al. 2015a), and Sicily (De Martini et al. 2012). Further traces have been recorded in Lakonia, Greece (Ntageretzis et al. 2015a), offshore of

Table 6 All high-energy event layers detected in the sediment cores within the Korission Lagoon with grain sizes, selected sedimentary features and, if available, radiocarbon ages

Event layer	Sediment core	Depth [m b.s.]	Grain size	Sedimentary features	Age
E1	LIN 1A	5.25–4.30	Medium to coarse sand	Erosional unconformity marine macrofossils	BC
E2	LIN 1A	3.59–2.98	Medium to fine sand	Erosional unconformity marine macrofossils	BC
E3	LIN 1A	1.33–0.34	Fine to medium sand	erosional unconformity marine macrofossils	389–110 cal BC (tadq/tpq)
E4	LIN 1A KOR 19	0.13–0.11 4.47–3.00	Fine sand medium to coarse sand	Erosional unconformity marine macrofossils marine macrofossils seaweed poorly sorted	Between 897–798 cal BC (tpq) and 347–620 cal AD (taq)
E5	KOR 19 KOR 20A KOR 21A	2.80–1.37 0.85–0.73 0.72–0.48	Medium sand in parts coarser/finer fine sand fine to medium sand	Marine macrofossils poorly sorted	Between 347–620 cal AD (tpq) and 1326–1426 cal AD/1283–1388 cal AD (taq)
E6	KOR 19 KOR 20A KOR 21A	1.18–0.15 0.60–0.39 0.38–0.29	Fine to medium sand fine sand fine to medium sand	Marine macrofossils	younger than 1326–1426 cal AD (tpq) and 1283–1388 cal AD (tpq)

Tunesia (Bahrouni et al. 2024), and along the coastline of Crete (Werner et al. 2018, 2019a, 2019b) where the epicentre of the earthquake was located (see Fig. 14 and Table 7).

For event V identified in sediment core KOR 19 (subunit E5), the radiocarbon age of 347–620 cal AD functions as a *terminus post quem* while the age obtained above the event V deposits, namely 1326–1426 cal AD (Fig. 13, Tables 4, 6), yields a *terminus ante quem*. Again, the age of the overlying lagoonal mud approximates the age of the event better due to erosion effects at the base of the event layer that are supposed to have produced a hiatus. The corresponding layer of event V can, therefore, neatly be attributed as candidate layer for the earthquake and tsunami of 1303 AD. This is confirmed by event deposits on the landward shore of the Korission Lagoon in sediment core KOR 20A that were dated to 1283–1388 cal AD (subunit E5, Fig. 13, Table 4). This age represents a *terminus ante quem* which also points to the 1303 AD tsunami. Sediment core KOR 21A shows a similar stratigraphy. We, thus, conclude that event V deposits were found on both the western and the landward shore of the Korission Lagoon and reflect the influence of high-energy tsunami inundation and

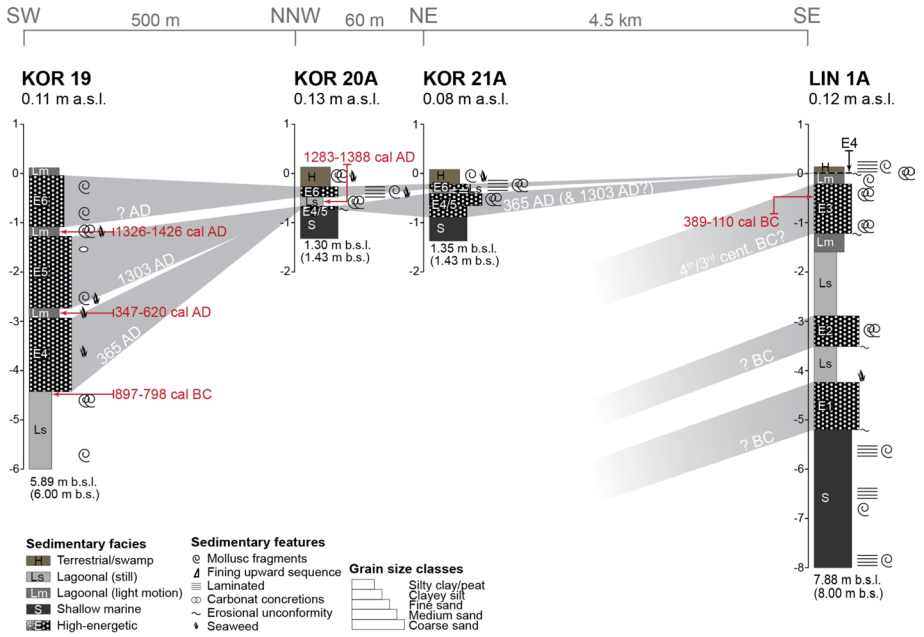

Fig. 13 Transect of sediment core drilled at the shores of the Korission Lagoon. Please refer to Fig. 2 for location of coring sites

associated sedimentary imprint of the entire lagoon by one and the same event. Radiocarbon ages from both shores make the 1303 AD tsunami the most probable candidate responsible for these sedimentary signatures.

These results match with multiple geomorphological and sedimentological evidence of the 1303 AD tsunami that were found along many coasts of the eastern Mediterranean during the past decades. Corresponding traces were also been found at the coasts of the Ambrakian Gulf and the Sound of Lefkada (Vött et al. 2006, 2007, 2009b), the Gulf of Kyparissia (Obrocki et al. 2020), the ancient harbour of Krane (Vött et al. 2014), and the Gialova Lagoon (Willershäuser et al. 2015b), and along the coasts of the southern and southeastern Peloponnese (Ntageretzis et al. 2015a, b, c; Scheffers et al. 2008), and Crete (Werner et al. 2019b). The 1303 AD event is also well documented in historical sources (Ambraseys 2009; Guidoboni and Comastri 1997; Papadopoulos et al. 2012).

Sediments of event VI were encountered in cores KOR 19, KOR 20A, and KOR 21A (Fig. 13). This event must have occurred after 1283–1388 cal AD which represents *terminus post quem* for it (Table 6). For the northern Ionian Sea and Corfu Island in particular, earthquake and tsunami catalogues mention two earthquakes and associated tsunami waves for this time period, one of which may have caused the input of high-energy deposits during event VI: One event occurred in 1732 (Ambraseys 2009; Papazachos and Dimitriu 1991; Partsch 1887) and another one in 1883 (Ambraseys 2009; Galanopoulos 2011). We, therefore, assume that event VI took place in the 18th or 19th cent. AD.

To sum up, sediment cores drilled along the western, eastern and southern shores of the Korission Lagoon revealed sedimentary signatures of six high-energy wave impacts which are interpreted to be associated with tsunami landfalls (see Table 6). Event signatures can be

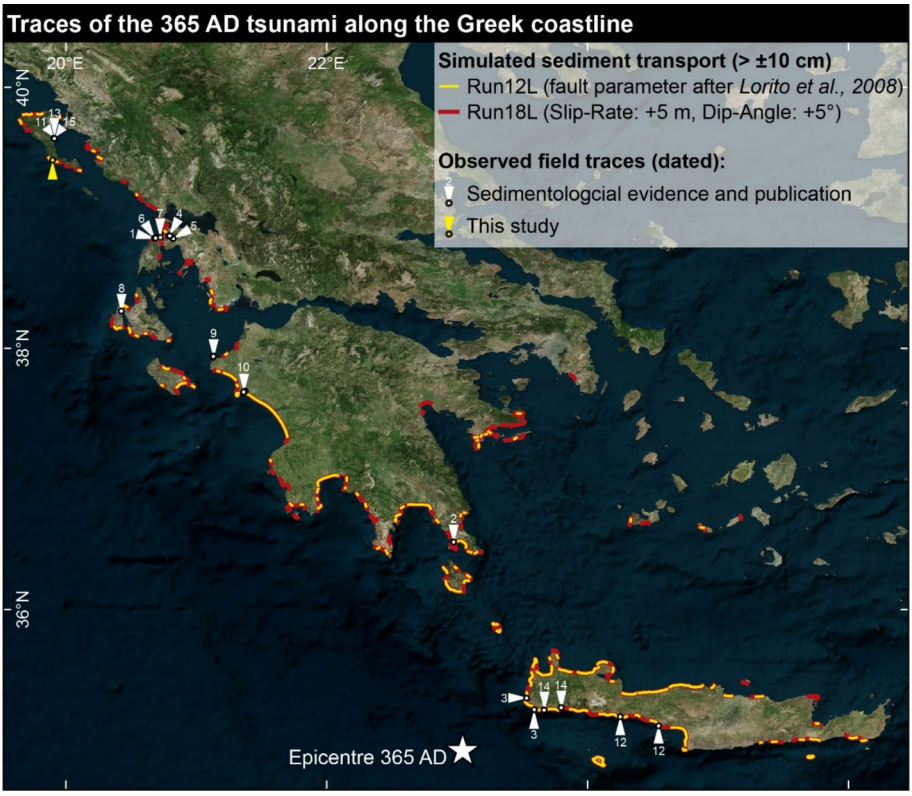

Fig. 14 Overview of the Greek coastline in the eastern Ionian Sea coastlines, the Cretan and Aegean Seas showing locations of geomorphological, sedimentological and geochronological field evidence for the landfall of the 365 AD tsunami (this study and literature review) in comparison with results of numerical simulation of the 365 AD tsunami (this study). Please refer to Table 7 for the corresponding references and ages. Red lines along the coast mark simulated sediment transport > ± 10 cm (Run12L–yellow line and Run18L–red line, Map: ©Microsoft, 2024)

classified into two groups. Traces of the three older events (I–III) were only found in core LIN 1A while the three younger events are most prominently documented in cores KOR 19, 20A and 21A. It seems as if the coastal configuration has changed between events III and IV so that the southern lagoonal shore became more remote and more protected with regard to younger events. This might be associated with co-seismic uplift of the southern shore at site LIN 1A related to event III. Evidence of co-seismic uplift and contemporaneous tsunami landfall for event III is already described by Finkler et al. (2018, 2019) for the Bay of Corfu at the eastern side of the island, namely for the ancient Alkinoos Harbour and the Pieri quay wall. Here, the island was uplifted by approximately 1.74 m in conjunction with an earthquake and tsunami in the 4th/3rd cent. BC.

The continuous sedimentation which is documented in the stratigraphy of sediment core KOR 19, however, suggests that the island has not experienced major uplift between the 4th cent. AD and modern times. Traces for the younger events dated to 365 AD, 1303 AD and the 18th or 19th cent. AD (events IV, V, and VI) were found in cores KOR 19, 20A and

Table 7 Geomorphological and sedimentological evidence of the 365 AD tsunami landfall found along coasts along of the eastern Mediterranean Sea

No	Publication	Location	Age		
			Dating in relation to event occurrence	Published Ages	Recalibrated ^{14}C Ages (2σ, Calib 8.2)
1	Vött et al. (2006)	Lagoon of Lefkada	tadq	387–472 cal AD (1σ)*	448–702 cal AD
2	Scheffers et al. (2008)	North of Elaphonisos Island, S Greece	tpq	134–380 cal AD (2σ)	246–526 cal AD
3	Shaw et al. (2008)	multiple locations on Crete Island and Greece	tadq corals and bryozoa species below uplifted palaeoshoreline	340–604 cal AD (2σ)* 282–565 cal AD (2σ)* 271–551 cal AD (2σ)* 159–428 cal AD (2σ)* 235–515 cal AD (2σ)* 284–564 cal AD (2σ)* 280–556 cal AD (2σ)* 352–608 cal AD (2σ)* 166–438 cal AD (2σ)* 288–570 cal AD (2σ)* 275–553 cal AD (2σ)*	432 – 685 cal AD* 409 – 664 cal AD* 393 – 656 cal AD* 263 – 558 cal AD* 340 – 621 cal AD* 409 – 664 cal AD* 405 – 661 cal AD* 439 – 690 cal AD* 182 – 483 cal AD* 412 – 666 cal AD* 400 – 659 cal AD*
4	Vött et al. (2008)	Aghios Nikolaos, NW Greece	tpq	224–348 cal AD (1σ)*	280–608 cal AD*
5	Vött et al. (2009a)	Lake Voulkaria, NW Greece	tpq/taq sandwich dating	Between 261–407 cal AD and 403–533 cal AD (1σ)	Between 246–529 cal AD and 267–565 cal AD
6	May et al. (2012a)	Gyra washover fan, NW Greece	tadq within washover deposits	349–533 cal AD (2σ)*	488–702 cal AD*
7	May et al. (2012b)	Lefkada Barrier, NW Greece	tadq dislocated beachrock slab	53–235 cal AD (2σ)*	157–458 cal AD*
8	Willershäuser et al. (2013)	Gulf of Argostoli	tpq/tadq	225–316 cal AD (1σ)*	324–603 cal AD*
9	Hadler et al. (2015a)	Kyllini, W Greece	tpq	40 cal BC–21 cal AD (1σ)	49 cal BC–104 cal AD
10	Willershäuser et al. (2015a)	Mouria Lagoon, W Greece	tpq	232–327 cal AD (1σ)*	301–596 cal AD*
11	Finkler et al. (2017)	Alkinoos Harbour, Corfu	tpq / tanq sandwich dating	Between 78–177 cal AD and 413–533 cal AD (1σ)	Between 77–218 cal AD and 419–539 cal AD
			tpq	236–325 cal AD (1σ)	231–362 cal AD
12	Boulton and Whitworth (2018)	Diplomo Petris and Lakki, Crete	tadq Serpulid from site	181–397 cal AD (2σ)*	249–544 cal AD*
13	Finkler et al. (2018)	Corcyra, Corfu	tpq	89 cal BC–1 cal AD (1σ)	147 cal BC–58 cal AD

Table 7 (continued)

No	Publication	Location	Age		
			Dating in relation to event occurrence	Published Ages	Recalibrated ^{14}C Ages (2σ, Calib 8.2)
14	Werner et al. (2018)	Sougia, Crete	tadq tsunamite	*1.42 ± 0.01 ka (OSL Ages)*	
		Palaiochora, Crete	tadq tsunamite	142–225 cal AD (1σ)* 260–348 cal AD (1σ)* 360–431 cal AD (1σ)* 361–431 cal AD (1σ)* *1.14 ± 0.1 ka (OSL Ages)*	227–516 cal AD 338–618 cal AD 429–676 cal AD 430–675 cal AD
15	Finkler et al. (2019)	Alkinoos Harbour, Corfu	tpq	7–69 cal AD and 27–117 cal AD (1σ)	37 cal BC–123 cal AD and 19–204 cal AD

^{14}C ages from original publications were recalibrated in Calib 8.2 using the IntCal20 or Marine20 (marked with *) curves (Heaton et al. 2020; Reimer et al. 2020). Confidence intervals used in the original publications are given in brackets. Recalibrated ages are given with a confidence interval of 2σ. Please note that the mean Marine Reservoir Effect considered by the Calib software changed from 400 to 550 years with the introduction of the IntCal20 and Marine20 curves (Heaton et al. 2020)

21A and represent (tele-)tsunami events that hit Corfu, and which are not related to local co-seismic crust movements.

5.4 Numerical simulation

In our model, the first wave generated by the 365 AD earthquake reaches the coastline after approximately 1:08 h and enters the Korission Lagoon in all scenarios. It is not the highest wave of the tsunami wave train (Fig. 15A1–C1) but the highest wave simulated for the 365 AD tsunami is within the first 10 waves (see also Röbke and Vött 2017). Due to wave shoaling, the highest waves can be observed on the seaward side of the lagoon and especially south of the palaeodunes in the southeast. Here, the dunes function as natural protection so marine waters cannot enter the lagoon from this side. On the contrary, the beach ridge separating the lagoon from the Ionian Sea in the west is already inundated by waves with smaller wave heights and, with advancing erosion of the ridge, the whole lagoon is affected by water masses entering from that side (Fig. 10A).

Increasing wave heights and high flow velocities lead to the erosion of beach ridge material that is subsequently washed into the lagoon building washover fans as geomorphological feature typical of high-energy events (Gianfreda et al. 2001; May et al. 2012a, b). The largest amounts of sediment are transported along the western beach ridge where highest flow velocities are simulated (Fig. 10B + C). Observation points in this area show an onset of sediment rearrangement with the first wave entering the lagoon (Fig. 15A + B). Here, the erosion of the beach ridge and sediment transport into the lagoon becomes visible in the alterations of the bottom level (Fig. 15A3 + B_3). Throughout the simulation, erosion and sedimentation occur in different steps which can be correlated with maximum values of both wave height (> 0.75 m) and flow velocity (> 2 ms^{-1}, Fig. 15A + B). Both processes take place in the same wave cycles: Decreasing flow velocity after overflowing the beach ridge causes a decrease in transport capacity, leading to an accumulation of sediment eroded from the beach ridge into the lagoon. Highest rates of sediment transport do not corre-

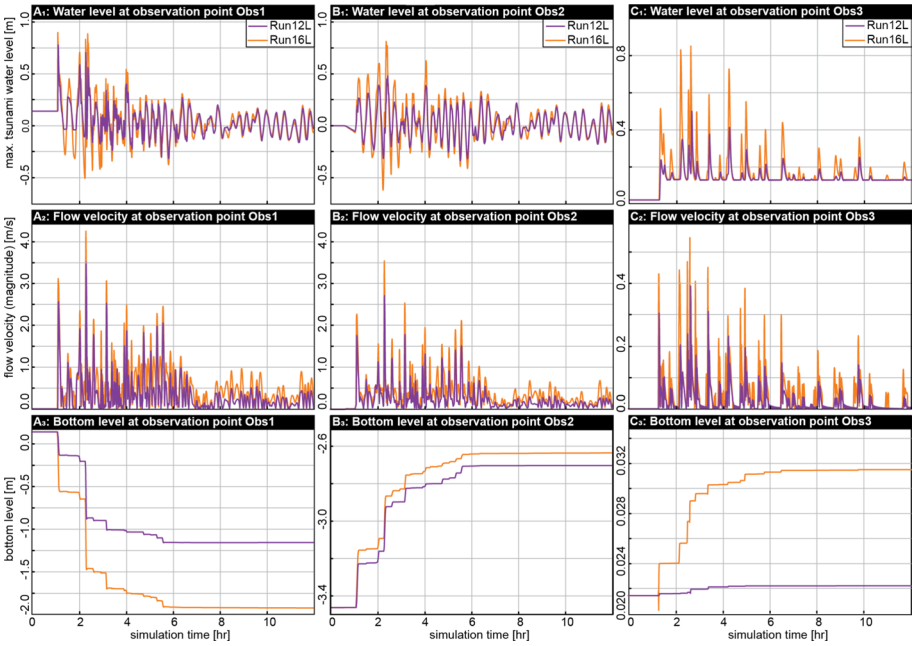

Fig. 15 Water level (top), flow velocity (middle), and bottom level (bottom) simulated for the 365 AD tsunami at observation points Obs1 (**A**) and Obs2 (**B**), both located on and near the beach ridge near KOR 19, and Obs3 (**C**) located near LIN 1A (for locations see Fig. 10)

spond to the highest values of the water level and flow velocity. Since sediment availability throughout the model domain is consistent, bathymetrical and topographical settings and their changes throughout the event seem to play a major role regarding the dimensions of sediment transport. In total, 1.3–2.07 m of sand is eroded from the beach ridge in the two different scenarios (Fig. 15A3), while 0.76 m–0.83 m are accumulated in the lagoon (Fig. 15B3). The remaining sediment is transported farther into the lagoon or, by backflow dynamics, back into the Ionian Sea, thus, building washover fans on both sides of the beach ridge. In general, all selected parameters increase with the adaptation of the slip rate of both seismic scenarios.

For the entire lagoon, the maximum water level reveals a funnelling effect (Fig. 10A, see also Röbke and Vött 2017): In the centre of the lagoon where it is widest the water level remains lower compared to both, the narrower northwestern and the southeastern ends of the lagoon. Therefore, an increase in wave height is observed for coring site LIN 1A which is located at the southern lagoonal shore. Even though the water level (< 1 m) and the flow velocity (< 0.6 m s^{-1}) are smaller compared to the beach ridge, they are sufficient to relocate sediment farther inland. Again, the sedimentation process takes place in cycles generally linked to maxima in water levels and flow velocities. The variation in the bottom level in the scenario based on Lorito et al. (2008) shows that erosion precedes a new sediment accumulation, especially in Run16L (Fig. 15C3).

Comparing the different seismic scenarios in terms of sediment transport, the rate of erosion on the beach ridge (Obs1) doubles with the model adaptation from Run12L (−1.3 m) to Run16L (−2.07 m, Table 5). In terms of sedimentation into the lagoon (Obs2), the dif-

ferences between the selected seismic scenarios are smaller (Run12L: +0.76 m, Run16L: +0.83 m). Since the transport is directed inland, it can be inferred that the lower sedimentation rates near the beach ridge in the adapted seismic scenarios are due to a wider spread of the available sediment into the lagoon with higher waves and increased velocities. This is supported by the extent of the washover fans which reach farther into the lagoon and back into the Ionian Sea in Run16L. At coring site LIN 1A, the sedimentation gradually increases with simulation time (Fig. 15C3). To sum up, a clear correlation between slip rate and sediment transport can be inferred: A higher slip rate leads to (i) higher flow velocities, (ii) an increase in erosion on the beach ridge, and (iii) washover fans reaching farther into the lagoon.

Regarding the numerical simulation of the 1303 AD tsunami, the first effects on the lagoon can be observed after almost 2 h simulation time (Fig. 16). During the simulation, both tsunami wave height and flow velocity remain relatively low. In fact, they remain too low to trigger erosion and sedimentation in the Korission Lagoon. In comparison with the simulation of the 365 AD tsunami, these reduced impacts can be ascribed (i) to the location of the assumed epicentre of the 1303 AD earthquake much further eastwards and to the propagation of the resulting tsunami waves more towards the east of the Mediterranean Sea (Fig. 9C), (ii) to an inaccuracy of the location of the epicentre itself or the fault parameter, and (iii) to the low slip rate of the fault (Table 1). A more detailed sensitivity analysis on these parameters needs to be carried out for a more precise conclusion which exceed the scope of this study.

5.5 Comparing field data with numerical simulation scenarios

The combination of numerical models and field traces helps to understand the evolution of the Korission Lagoon in the context of extreme wave impact. For the numerical simulation, it is essential to consider that spatial and temporal model discretisation result in a loss of information on the wave and sediment dynamics as well as other parameters. Due to this discretisation error and due to the given uncertainty of the model (input) parameters such as the initial tsunami water levels, applied roughness coefficient, and the considered sediment fraction, any model only gives an approximation to the actual conditions (Röbke and Vött 2017). However, in case of the 365 AD tsunami simulations, the results obtained for sediment erosion and accumulation give rather concrete information on the formation dynamics of the washover fans observed at the western lagoonal shore. With several waves higher than 0.4 m, sediment is eroded from the beach ridge and relocated into the lagoon and, during backflow, into the Ionian Sea. The washover fans in the latter have most likely been reworked by alongshore currents during the following years or decades. On the contrary, for the washover fans developed in the lagoon, simulation results show a gradual increase of the bottom level through accumulation of sediments without signs of erosion in the lagoon (KOR 19).

Contrary to coring site of KOR 19 where only sedimentation of the eroded material from the beach ridge can be observed, erosion becomes apparent prior to most cycles of sediment accumulation at coring site LIN 1A. This fits well with the field data: While the stratigraphic record of core KOR 19 does not show signs of erosion, high-energy deposits found in core LIN 1A are always associated with a basal erosional unconformity. This phenomenon can also be observed for the lowest event deposits of KOR 20A (subunit E4/E5, event IV/V,

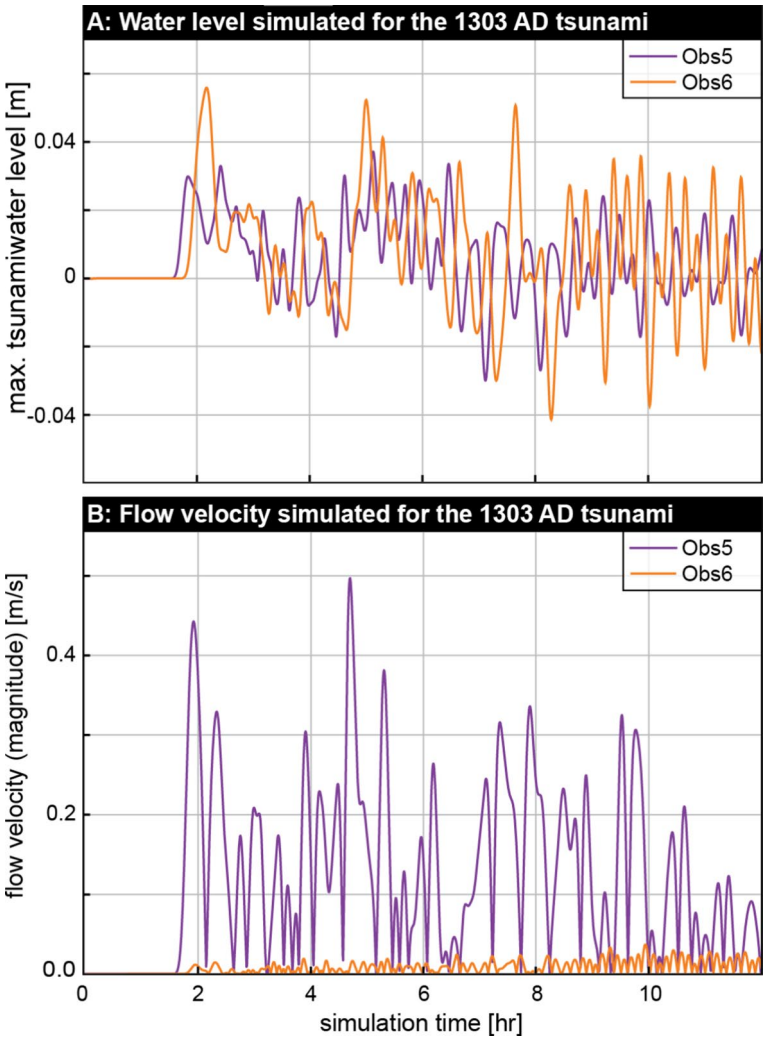

Fig. 16 Water level (**A**) and flow velocity (**B**) simulated for the 1303 AD tsunami at observation points Obs5 on the beach ridge near KOR 19 and Obs6 near coring site of LIN 1A (for locations see Fig. 10)

Fig. 13) and indicates the high impact of the event on the coastline, leading to sediment flow into the lagoon and, hence, forming the washover fans. The thickness of the event deposits deduced from numerical simulation is consistent with the actual thickness found in the field: the model shows up to 1.1 cm of sand while 2 cm of fine sandy deposits were found in sediment core LIN 1A. Regarding the washover fan at the western lagoonal shore, 1.34 m of medium sand was found in core KOR 19, whereas the numerical simulation yielded sediment accumulation of up to 0.83 m. The simulation results also confirm a loss of energy and the resulting decrease of sediment relocation towards the landward coastlines of the lagoon as found in the sedimentary record. Near coring sites KOR 20A and KOR 21A, a sediment

accumulation of only 0.4 m was simulated (Figs. 10, 11, 15). Although there is a difference of several decimetres in the sediment accumulation rates, the general dimension is reliable.

By varying the depth of the lagoon within the numerical simulation and comparing the results with field traces, the model also helps to understand the influence of tectonic factors and sea level changes: The best-fit accordance between simulated and observed sediment accumulation at the lagoonal shore was found for a lagoonal water depth of 4 m. This corresponds with the lowest high-energy deposits found in sediment core KOR 19 which is suggested to represent the 365 AD tsunami equivalent (Figs. 6, 13). The subsequent sedimentation of lagoonal muds intercalated with high-energy deposits found in the field data reflect an undisturbed depositional environment (Figs. 6, 15B3). Therefore, it seems as if the Korission Lagoon has been tectonically stable at least since the fourth century AD and sedimentation occurred at a similar rate as sea level rise. This is in accordance with previous studies on Corfu Island which only dated considerable seismo-tectonic movements prior to the 3rd cent. BC (Evelpidou et al. 2014; Finkler et al. 2018; Georg et al. 2022; Mastronuzzi et al. 2014).

For the landward lagoonal shore at coring sites KOR 20A and 21A, erosion and sedimentation were simulated in Run12L and Run18L. The thickness of the deposits does not exceed 1.8 cm which is less than the observed 7 cm and 54 cm of sediment found in cores KOR 20A and KOR 21A, respectively. Still, it needs to be considered that the increase in the slip rate and dip angle in Run16L and Run18L leads to a greater extent of the washover fans which also suggests that it can reach the opposing coastline (Fig. 11). For both sediment cores, radiocarbon data imply that these layers are associated to the 1303 AD tsunami. This younger tsunami impact may have eroded and reworked 365 AD tsunami deposits.

The results suggest that, for Corfu Island, existing slip rates are underestimated. The same can be observed for other locations in the Ionian Sea: In the Bay of Aghios Nikolaos and Lake Voulkaria, field evidence of the 365 AD event have been described (May et al. 2012a, b; Vött et al. 2008, 2009a) but only an increase in the fault parameters lead to a sediment relocation in this area (Fig. 14, Table 7). For other locations closer to the epicentre of the earthquake, the differences between the runs are less distinct. In general, the correlation between field traces and simulated sediment transport along the Greek coastline is apparent. Therefore, the simulation results might help to identify undated tsunami sediments and allow to ascribe their origin to the 365 AD event.

The 1303 AD tsunami simulation does not show any sediment accumulation in the Korission Lagoon, neither in the presented results nor in the sensitivity runs (not shown) performed for the study area. Similar to the approach for the 365 AD tsunami, these sensitivity runs were based on the variation of the slip rate, and changes in the topography of both, the height of the beach ridge and the depth of the lagoon. Additionally, possible 1303 AD tsunami deposits observed in the realm of the Korission Lagoon may have been caused by multiple high-energy events. In the light of geoscientific evidence of associated event deposits presented in this study, the missing traces in the simulation can hint to a necessary adaptation of both, the topography of the lagoon and the fault parameters (see also Sect. 5.5). The results imply that the earthquake mechanisms might be underestimated in the existing literature or it might support the hypothesis of a series of tsunamigenic earthquakes with a resulting higher total tsunami wave height (e.g., El-Sayed et al. 2000; Pagnoni et al. 2015).

Still, the results of our study help to understand the correlation between tsunami wave height and sedimentation for the 365 AD event. By implementing a hydrodynamic model

and validating it with field data, we are able to show that it is not possible to infer thickness of tsunami deposits solely from the maximum tsunami wave heights. Our results rather underline the importance of the local geomorphological setting and the use of a high-resolution model for the areas of interest as also suggested by Bahrouni et al. (2024). The washover fans that were formed on the seaward side of the beach ridge have been reworked and disappeared while their counterparts on the lagoonal side remained visible.

6 Conclusions

In this study, we reconstructed the evolution of the Korission Lagoon, Corfu Island, from a sheltered shallow marine bay to the recent lagoon. This evolution has been triggered and then repeatedly been interrupted by high-energy events. Washover fans within the lagoon represent geomorphological traces of these events which are accompanied by multiple layers of allochthonous marine sands and basal erosional unconformities. Microfaunal and geochemical analyses verify these findings and allow identifying the allochthonous marine sediments within the in situ lagoonal sedimentary record.

Three older events (I–III) are recorded in sediments of the southern lagoonal shore. Event III is possibly identical with a local earthquake and tsunami event that affected Corfu Island during the 4th/3rd cent. BC and was found associated with co-seismic uplift (Finkler et al. 2018, 2019). Co-seismic uplift would also explain a major change in the coastal configuration as there are only weak signals of younger events at the southeastern lagoonal shore. The younger events are clearly documented in the sediment cores retrieved from the western and northern coastlines of the Korission Lagoon. Radiocarbon ages allow to correlate event IV found in KOR 19 with the 365 AD tsunami. Subsequent sedimentary traces of event V are candidates for the 1303 AD tsunami event.

The potential impact of the 365 AD tsunami on the western lagoonal shore was compared with modelling approaches presented in this paper. We were able to show the formation of washover fans by multiple wave cycles and with adaptations of the topography and the fault parameters. Moreover, we found good agreement between field data and simulation results. In the model, the sediment transport is related to water level peaks and flow velocity of single tsunami waves. However, no clear correlation between the three parameters can be inferred: The highest waves do not always correspond to highest flow velocities and largest sediment transport. Our model also verified inflowing processes that form erosional unconformities. Finally, we were able to show that an increase of slip rates and dip angles leads to an increase of tsunami wave height, flow velocities, sediment transport, and an enhanced impact on the lagoon as well as the coastlines of the Ionian Sea.

Our simulation results did not show any relocation of sediments in the lagoon during the 1303 AD event, even though corresponding traces were identified in sediment cores on both, the western and northern shores of the lagoon. Regarding the simulation approach, it, therefore, seems as if the fault parameters are underestimated and the location of the epicentre must be reconsidered. Our results show that further research is needed for the 1303 AD event especially concerning the source parameters, the potential role of several tsunami events resulting in washover fan formation and the contemporary topography. The youngest high-energy event, event VI, found in the sedimentary record of the Korission Lagoon can most probably be ascribed to a historical event in the 18th or nineteenth century AD. Pos-

sible candidates are the 1732 and 1883 earthquake with their epicentre on Corfu Island itself (e.g., Ambraseys, 2009; Galanopoulos 2011).

In general, our study shows the control function of the local geomorphological setting with regard to tsunami impacts as well as the great potential of lagoons for (palaeo-)tsunami research. It demonstrates that numerical morphodynamic models can successfully be applied for a comparison with historical tsunami events, provided that tsunami deposits are well-preserved and sufficient information on the tsunami trigger mechanism is available. The model set-up can help to improve future risk assessment for events similar to the 365 AD tsunami by assessing maximum tsunami water levels and associated inundation areas.

Supplementary Information The online version contains supplementary material available at https://doi.org/10.1007/s11069-025-07880-2.

Acknowledgements The study was realized within the framework of an interdisciplinary project directed by the Ephorate of Antiquities, Corfu, in collaboration with the Institute of Geography at the Johannes Gutenberg-Universität at Mainz, Germany, and the Centre Camille Jullian, CNRS at the Aix-Marseille Université, France. We are kindly indebted to the directorate and the personnel of the Ephorate of Antiquities of Corfu for their help and support. We also thank the Institute for Geology and Mineral Exploration (IGME, Athens) for issuing work permits.

Author contributions Funding acquisition: Andreas Vött, Peter Fischer; Supervision: Andreas Vött, Kalliopi Baika; Project administration: Andreas Vött, Peter Fischer, Kalliopi Baika; Data acquisition: Andreas Vött, Peter Fischer, Peter Frenzel, Timo Willershäuser; Numerical simulation: Tina Georg, Björn R. Röbke; Visualization: Tina Georg; Writing of original draft: Tina Georg; Writing (review and editing): Andreas Vött, Peter Fischer, Björn R. Röbke, Tina Georg.

Funding Open Access funding enabled and organized by Projekt DEAL. The project was funded by the Deutsche Forschungsgemeinschaft (DFG, Project number 280180719).

Declarations

Competing interests The authors declare that they have no conflict of interest.

References

Alexopoulos JD, Tomara V, Vassilakis Em, Papadopoulos TD, Dassenakis M, Poulos S, Voulgaris N, Dilalos S, Ghionis G, Goumas G, Pirlis E (2007) A contribution to environmental research of the Korissia coastal wetland (Corfu isl., Greece), with the application of combined geological and geophysical methods supported by Geographic Information Systems. Bull Geol Soc Greece 40:1892–1903. https://doi.org/10.12681/bgsg.17187

Ambraseys N (2009) Earthquakes in the mediterranean and middle east – a multidisciplinary study of seismicity up to 1900, 1st edn. Cambridge University Press, England. https://doi.org/10.1017/CBO9781139195430

Bahrouni N, Meghraoui M, Bayraktar HB, Lorito S, Zagrarni MF, Polonia A, Bel Mabrouk N, Kamoun F (2024) Tsunami deposits in Tunisia contemporaneous of the large 365 CE Crete earthquake and Mediterranean Sea catastrophic event. Sci Rep 14:4537. https://doi.org/10.1038/s41598-024-53225-7

Boulton SJ, Whitworth MRZ (2018) Block and boulder accumulations on the southern coast of Crete (Greece): evidence for the 365 CE tsunami in the Eastern Mediterranean. In: Scourse EM, Chapman NA, Tappin DR, Wallis SR (eds) Tsunamis: geology, hazards and risks, vol 456. Geological Society, Special Publications, London, pp 105–125. https://doi.org/10.1144/SP456.4

Brouwer P (2003) Theory of XRF: getting acquainted with the principles, 3rd edn. PANalytical BV, Almelo

Chabrol A, Stephan P, Apostolopoulos G, Pavlopoulos K, Gonnet A, Fouache E (2025) Mid-to late Holocene palaeogeographic evolution of the Kalamas river delta, Epirus (Thesprotia), Greece. Quat Sci Adv 17:100264. https://doi.org/10.1016/j.qsa.2024.100264

Chagué-Goff C (2010) Chemical signatures of palaeotsunamis: a forgotten proxy? Mar Geol 271:67–71. https://doi.org/10.1016/j.margeo.2010.01.010

Chagué-Goff C, Andrew A, Szczuciński W, Goff J, Nishimura Y (2012) Geochemical signatures up to the maximum inundation of the 2011 Tohoku-oki tsunami–implications for the 869 AD Jogan and other palaeotsunamis. Sediment Geol 282:65–77. https://doi.org/10.1016/j.sedgeo.2012.05.021

Chagué-Goff C, Chan JCH, Goff J, Gadd P (2016) Late Holocene record of environmental changes, cyclones and tsunamis in a coastal lake, Mangaia, Cook Islands. Island Arc 25:333–349. https://doi.org/10.1111/iar.12153

Chagué-Goff C, Schneider J-L, Goff JR, Dominey-Howes D, Strotz L (2011) Expanding the proxy toolkit to help identify past events–lessons from the 2004 Indian Ocean Tsunami and the 2009 South Pacific Tsunami. Earth-Sci Rev 107:107–122. https://doi.org/10.1016/j.earscirev.2011.03.007

Clemmensen LB, Bendixen M, Hede MU, Kroon A, Nielsen L, Murray AS (2014) Morphological records of storm floods exemplified by the impact of the 1872 Baltic storm on a sandy spit system in south-eastern Denmark. Earth Surf Process Landforms 39:499–508. https://doi.org/10.1002/esp.3466

Costa PJM, Leroy SAG, Dinis JL, Dawson AG, Kortekaas S (2012) Recent high-energy marine events in the sediments of Lagoa de Óbidos and Martinhal (Portugal): recognition, age and likely causes. Nat Hazards Earth Syst Sci 12:1367–1380. https://doi.org/10.5194/nhess-12-1367-2012

Darlas A, Karkanas P, Palli O, Papadea A (2006) Palaeolithic research on southwest Corfu. Athens Ann Archaeol 39:11–30

Dearing J (1999) Environmental Magnetic Susceptibility: using the Bartington MS2 system, 2nd edn. Bartington Instruments, England

Deltares: Delft3D. Simulation of multi-dimensional hydrodynamic flows and transport phenomena, including sediments. User Manual, Version: 4.05, 2024.

De Martini PM, Barbano MS, Pantosti D, Smedile A, Pirrotta C, Del Carlo P, Pinzi S (2012) Geological evidence for paleotsunamis along eastern Sicily (Italy): an overview. Nat Hazards Earth Syst Sci 12:2569–2580. https://doi.org/10.5194/nhess-12-2569-2012

De Martini PM, Bruins HJ, Feist L, Goodman-Tchernov BN, Hadler H, Lario J, Mastronuzzi G, Obrocki L, Pantosti D, Paris R, Reicherter K, Smedile A, Vött A (2021) The Mediterranean Sea and the Gulf of Cadiz as a natural laboratory for paleotsunami research: recent advancements. Earth-Sci Rev 216:103578. https://doi.org/10.1016/j.earscirev.2021.103578

Diakakis M, Mavroulis S, Filis C, Lozios S, Vassilakis E, Naoum G, Soukis K, Konsolaki A, Kotsi E, Theodorakatou D, Skourtsos E, Kranis H, Gogou M, Spyrou NI, Katsetsiadou K-N, Lekkas E (2023) Impacts of Medicanes on geomorphology and infrastructure in the Eastern Mediterranean, the case of Medicane Ianos and the Ionian Islands in Western Greece. Water 15:1026. https://doi.org/10.3390/w15061026

DIN ISO 11277 (2020) Bodenbeschaffenheit–Bestimmung der Partikelgrößenverteilung in Mineralböden–Verfahren mittels Sieben und Sedimentation. Beuth Verlag GmbH, Berlin

El-Sayed A, Romanelli F, Panza G (2000) Recent seismicity and realistic waveforms modeling to reduce the ambiguities about the 1303 seismic activity in Egypt. Tectonophysics 328:341–357. https://doi.org/10.1016/S0040-1951(00)00172-4

Evelpidou N, Karkani A, Pirazzoli PA (2014) Fossil shorelines at Corfu and surrounding islands deduced from erosional notches. Holocene 24:1565–1572. https://doi.org/10.1177/0959683614544057

Finkler C, Baika K, Rigakou D, Metallinou G, Fischer P, Hadler H, Emde K, Vött A (2018) Geoarchaeological investigations of a prominent quay wall in ancient Corcyra–implications for harbour development, palaeoenvironmental changes and tectonic geomorphology of Corfu Island (Ionian Islands, Greece). Quat Int 473:91–111. https://doi.org/10.1016/j.quaint.2017.05.013

Finkler C, Baika K, Rigakou D, Metallinou G, Fischer P, Hadler H, Emde K, Vött A (2019) The sedimentary record of the Alkinoos Harbour of ancient Corcyra (Corfu Island, Greece) – geoarchaeological evidence for rapid coastal changes induced by co-seismic uplift, tsunami inundation and human interventions. Zeitschrift Für Geomorphol Suppl Issues 62:197–246. https://doi.org/10.1127/zfg_suppl/2018/0514

Finkler C, Fischer P, Baika K, Rigakou D, Metallinou G, Hadler H, Vött A (2017) Tracing the Alkinoos Harbor of ancient Kerkyra, Greece, and reconstructing its paleotsunami history. Geoarchaeology 33:24–42. https://doi.org/10.1002/gea.21609

Fischer P, Finkler C, Röbke BR, Baika K, Hadler H, Willershäuser T, Rigakou D, Metallinou G, Vött A (2016b) Impact of Holocene tsunamis detected in lagoonal environments on Corfu (Ionian Islands, Greece): geomorphological, sedimentary and microfaunal evidence. Quat Int 401:4–16. https://doi.org/10.1016/j.quaint.2015.07.019

Fischer P, Wunderlich T, Rabbel W, Vött A, Willershäuser T, Baika K, Rigakou D, Metallinou G (2016a) Combined electrical resistivity tomography (ERT), direct-push electrical conductivity (DP-EC) logging and coring – a new methodological approach in geoarchaeological research. Archaeol Prospect 23:213–228. https://doi.org/10.1002/arp.1542

Flouri ET, Kalligeris N, Alexandrakis G, Kampanis NA, Synolakis CE (2013) Application of a finite difference computational model to the simulation of earthquake generated tsunamis. Appl Numer Math 67:111–125. https://doi.org/10.1016/j.apnum.2011.06.003

Fouache E, Ghilardi M, Vouvalidis K, Syrides G, Styllas M, Kunesch S, Stiros S (2008) Contribution on the Holocene Reconstruction of Thessaloniki Coastal Plain, Greece. J Coast Res 245:1161–1173. https://doi.org/10.2112/06-0786.1

Gaertner MÁ, González-Alemán JJ, Romera R, Domínguez M, Gil V, Sánchez E, Gallardo C, Miglietta MM, Walsh KJE, Sein DV, Somot S, Dell'Aquila A, Teichmann C, Ahrens B, Buonomo E, Colette A, Bastin S, van Meijgaard E, Nikulin G (2018) Simulation of medicanes over the Mediterranean Sea in a regional climate model ensemble: impact of ocean–atmosphere coupling and increased resolution. Clim Dyn 51:1041–1057. https://doi.org/10.1007/s00382-016-3456-1

Galanopoulos AG (2011) Tsunamis observed on the coasts of Greece from antiquity to present time. Ann Geophys 13:369–386. https://doi.org/10.4401/ag-5477

GEBCO Bathymetric Compilation Group (2019) The GEBCO_2019 Grid–a continuous terrain model of the global oceans and land. https://doi.org/10.5285/836f016a-33be-6ddc-e053-6c86abc0788e

Georg T, Obrocki L, Fischer P, Willershäuser T, Röbke BR, Baika K, Vött A (2022) Traces of Holocene extreme wave events in the Alykes coastal plain, Corfu Island, Zeitschrift für Geomorphologie, Special Issue. Geoarchaeology 1–22:2024. https://doi.org/10.1127/zfg/2024/0789

Gianfreda F, Mastronuzzi G, Sansò P (2001) Impact of historical tsunamis on a sandy coastal barrier: an example from the northern Gargano coast, southern Italy. Nat Hazards Earth Syst Sci 1:213–219. https://doi.org/10.5194/nhess-1-213-2001

Goff J (2008) Tsunami hazard assessment for Hawke's Bay region. NIWA Client Report, CH2008–021, 30

Goff J, Chagué C, Nichol S, Jaffe B, Dominey-Howes D (2012) Progress in palaeotsunami research. Sediment Geol 243:70–88. https://doi.org/10.1016/j.sedgeo.2011.11.002

Guidoboni E, Comastri A (1997) The large earthquake of 8 August 1303 in Crete: seismic scenario and tsunami in the Mediterranean area. J Seismol 1:55–72. https://doi.org/10.1023/A:1009737632542

Guidoboni E, Comastri A, Traina G (1994) Catalogue of ancient earthquakes in the Mediterranean area up to the 10th century. Istituto nazionale di geofisica, Rome, p 504

Hadler H, Baika K, Pakkanen J, Evangelistis D, Emde K, Fischer P, Ntageretzis K, Röbke B, Willershäuser T, Vött A (2015a) Palaeotsunami impact on the ancient harbour site Kyllini (western Peloponnese, Greece) based on a geomorphological multi-proxy approach. Zeitschrift Für Geomorphol Suppl Issues 59:7–41. https://doi.org/10.1127/zfg_suppl/2014/S-00187

Hadler H, Vött A, Fischer P, Ludwig S, Heinzelmann M, Rohn C (2015b) Temple-complex post-dates tsunami deposits found in the ancient harbour basin of Ostia (Rome, Italy). J Archaeol Sci 61:78–89. https://doi.org/10.1016/j.jas.2015.05.002

Hadler H, Willershääuser T, Ntageretzis K, Henning P, Vöött A (2012) Catalogue entries and non-entries of earthquake and tsunami events in the Ionian Sea and the Gulf of Corinth (eastern Mediterranean, Greece) and their interpretation with regard to palaeotsunami research. In: Beiträäge der 29. Jahrestagung des Arbeitskreises "Geographie derMeere und Küüsten", 28. bis 30. April 2011 in Bremen, pp 1–15

Haenssler E, Unkel I, Döörfler W, Nadeau MJ (2014) Driving mechanisms of Holocene lagoon development and barrier accretion in Northern Elis, Peloponnese, inferred from the sedimentary record of the Kotychi Lagoon. E&G Quat Sci J 63:60–77. https://doi.org/10.3285/eg.63.1.04

Hamouda AZ (2006) Numerical computations of 1303 tsunamigenic propagation towards Alexandria, Egyptian Coast. J Afr Earth Sci 44:37–44. https://doi.org/10.1016/j.jafrearsci.2005.11.005

Hamouda AZ (2010) Worst scenarios of tsunami effects along the Mediterranean coast of Egypt. Mar Geophys Res 31:197–214. https://doi.org/10.1007/s11001-010-9099-4

Harrington GA, Hendry MJ (2006) Using direct-push EC logging to delineate heterogeneity in a clay-rich aquitard. Groundwater Monit Remediat 26:92–100. https://doi.org/10.1111/j.1745-6592.2006.00063.x

Heaton TJ, Köhler P, Butzin M, Bard E, Reimer RW, Austin WEN, Bronk Ramsey C, Grootes PM, Hughen KA, Kromer B, Reimer PJ, Adkins J, Burke A, Cook MS, Olsen J, Skinner LC (2020) Marine20—the marine radiocarbon age calibration curve (0–55,000 cal BP). Radiocarbon 62:779–820. https://doi.org/10.1017/RDC.2020.68

IGME, I. of G. and M. E (1970) Geological Map of Greece e Sheet North and South Corfu, Athens, Greece

International seismological centre (2025) On-line bulletin. https://doi.org/10.31905/D808B830

Jamaluddin and Umar, E. P. (2018) Identification of subsurface layer with Wenner-Schlumberger arrays configuration geoelectrical method. IOP Conf Ser Earth Environ Sci 118:012006

Jarvis A, Reuter HI, Nelson A, Guevara E (2008) Hole-filled seamless SRTM data V4

Kalnicky DJ, Singhvi R (2001) Field portable XRF analysis of environmental samples. J Hazard Mater 83:93–122. https://doi.org/10.1016/S0304-3894(00)00330-7

Köhn M (1929) Korngrößenbestimmung vermittels Pipettanalyse. Tonindustrie-Ztg 55:729–731

Kortekaas S, Dawson AG (2007) Distinguishing tsunami and storm deposits: an example from Martinhal SW Portugal. Sediment Geol 200:208–221. https://doi.org/10.1016/j.sedgeo.2007.01.004

Lionello P, Cogo S, Galati MB, Sanna A (2008) The Mediterranean surface wave climate inferred from future scenario simulations. Glob Planet Change 63:152–162. https://doi.org/10.1016/j.gloplacha.2008.03.004

Liu Q, Roberts AP, Larrasoaña JC, Banerjee SK, Guyodo Y, Tauxe L, Oldfield F (2012) Environmental magnetism: principles and applications. Rev Geophys 50:RG4002. https://doi.org/10.1029/2012RG000393

Loeblich AR Jr, Tappan H (1988) Foraminiferal genera and their classification. Springer US, New York

Loke MH, Barker RD (1996) Rapid least-squares inversion of apparent resistivity pseudosections by a quasi-Newton method. Geophys Prospect 44:131–152

Lorito S, Tiberti MM, Basili R, Piatanesi A, Valensise G (2008) Earthquake-generated tsunamis in the Mediterranean Sea: scenarios of potential threats to Southern Italy. J Geophys Res 113:B01301. https://doi.org/10.1029/2007JB004943

Mastronuzzi G, Calcagnile L, Pignatelli C, Quarta G, Stamatopoulos L, Venisti N (2014) Late Holocene tsunamogenic coseismic uplift in Kerkira Island, Greece. Quat Int 332:48–60. https://doi.org/10.1016/j.quaint.2013.10.042

May SM, Vött A, Brückner H, Grapmayer R, Handl M, Wennrich V (2012b) The Lefkada barrier and beachrock system (NW Greece)–controls on coastal evolution and the significance of extreme wave events. Geomorphology 139:330–347. https://doi.org/10.1016/j.geomorph.2011.10.038

May SM, Vött A, Brückner H, Smedile A (2012a) The Gyra washover fan in the Lefkada Lagoon, NW Greece – possible evidence of the 365 AD Crete earthquake and tsunami. Earth Planets Space 64:859–874. https://doi.org/10.5047/eps.2012.03.007

Municipality of Corfu: Open Data Corfu: DEM Mapsheets, 2017

Murray JW (1991) Ecology and paleoecology of benthic foraminifera. Longman Scientific & Technical, Harlow, p 397

Murray JW (2006) Ecology and application of benthic foraminifera. Cambridge University Press, Cambridge, p 440

Ntageretzis K, Vött A, Emde K, Fischer P, Hadler H, Röbke BR, Willershäuser T (2015a) Palaeotsunami record in near-coast sedimentary archives in southeastern Lakonia (Peloponnese, Greece). Zeitschrift Für Geomorphol Suppl Issues 59:275–299. https://doi.org/10.1127/zfg_suppl/2015/S-00208

Ntageretzis K, Vött A, Fischer P, Hadler H, Emde K, Röbke BR, Willershäuser T (2015b) Traces of repeated tsunami landfall in the vicinity of Limnothalassa Moustou (Gulf of Argolis – Peloponnese, Greece). Zeitschrift Für Geomorphol Suppl Issues 59:301–317. https://doi.org/10.1127/zfg_suppl/2015/S-00206

Ntageretzis K, Vöött A, Fischer P, Hadler H, Emde K, Röobke BR, Willershääuser T (2015c) Palaeotsunami history of the Elos Plain (Evrotas River delta, Peloponnese, Greece). Zeitschrift füür Geomorphologie. Suppl Issue 59:253–273. https://doi.org/10.1127/zfg_suppl/2015/S-00207

Obrocki L, Vöött A, Wilken D, Fischer P, Willershääuser T, Koster B, Lang F, Papanikolaou I, Rabbel W, Reicherter K (2020) Tracing tsunami signatures of the AD 551 and AD 1303 tsunamis at the Gulf of Kyparissia (Peloponnese, Greece) using direct push in situ sensing techniques combined with geophysical studies. Sedimentology 67:1274–1308. https://doi.org/10.1111/sed.12555

Ott RF, Wegmann KW, Gallen SF, Pazzaglia FJ, Brandon MT, Ueda K, Fassoulas C (2021) Reassessing Eastern Mediterranean tectonics and earthquake hazard from the 365 CE earthquake. AGU Adv. https://doi.org/10.1029/2020AV000315

Pagnoni G, Armigliato A, Tinti S (2015) Scenario-based assessment of buildings' damage and population exposure due to earthquake-induced tsunamis for the town of Alexandria. Egypt Nat Hazards Earth Syst Sci 15:2669–2695. https://doi.org/10.5194/nhess-15-2669-2015

Papadimitriou EE, Karakostas VG (2008) Rupture model of the great AD 365 Crete earthquake in the southwestern part of the Hellenic Arc. Acta Geophys 56:293–312. https://doi.org/10.2478/s11600-008-0001-6

Papadopoulos GA, Daskalaki E, Fokaefs A, Giraleas N (2007) Tsunami hazards in the Eastern Mediterranean: strong earthquakes and tsunamis in the East Hellenic Arc and Trench system. Nat Hazards Earth Syst Sci 7:57–64. https://doi.org/10.5194/nhess-7-57-2007

Papadopoulos GA, Fokaefs A (2005) Strong tusnamis in the mediterranean sea: a re-evaluation. ISET J Earthq Technol 42:159–170

Papadopoulos GA, Minoura K, Imamura F, Kuran U, Yalçiner A, Fokaefs A, Takahashi T (2012) Geological evidence of tsunamis and earthquakes at the Eastern Hellenic Arc: correlation with historical seismicity in the eastern Mediterranean Sea. Res Geophys 2:12. https://doi.org/10.4081/rg.2012.e12

Papazachos BC, Dimitriu PP (1991) Tsunamis in and near Greece and their relation to the earthquake focal mechanisms. Nat Hazard 4:161–170

Partsch J (1887) Die Insel Korfu. In: Eine geographische Monographie. Gotha, p 108

Pirazzoli PA, Comment J, Thommer Y, Laborel J, Montag LF (1982) Crustal block movements from Holocene shorelines: Crete and Antikythira (Greece). Tectonophysics 86:27–43

Pirazzoli PA, Stiros SC, Laborel J, Laborel-Deguen F, Arnold M, Papageorgiou S, Morhange C (1994) Late-Holocene shoreline changes related to palaeoseismic events in the Ionian Islands, Greece. Holocene 4:397–405. https://doi.org/10.1177/095968369400400407

Profe J, Zolitschka B, Schirmer W, Frechen M, Ohlendorf C (2016) Geochemistry unravels MIS 3/2 paleoenvironmental dynamics at the loess–paleosol sequence Schwalbenberg II. Ger Palaeogeogr Palaeoclimatol Palaeoecol 459:537–551. https://doi.org/10.1016/j.palaeo.2016.07.022

Pytharoulis I, Craig G, Ballard S (2000) The hurricane-like Mediterranean cyclone of January 1995. Meteorol Appl 7:261–279

Röbke BR, Leijnse T, Winter G, van Ormondt M, van Nieuwkoop J, de Graaff R (2021) Rapid assessment of tsunami offshore propagation and inundation with D-FLOW flexible mesh and SFINCS for the 2011 Tōhoku Tsunami in Japan. J Mar Sci Eng 9:453. https://doi.org/10.3390/jmse9050453

Röbke BR, Vött A (2017) The tsunami phenomenon. Prog Oceanogr 159:296–322

Röbke BR, Vött A, Willershäuser T, Fischer P, Hadler H (2015) Considering coastal palaeogeographical changes in a numerical tsunami model–a progressive base to compare simulation results with field traces from three coastal settings in western Greece. Int J Earth Sci 2006:463–490. https://doi.org/10.1127/zfg_suppl/2014/S-00210

Reimer PJ, Austin WEN, Bard E, Bayliss A, Blackwell PG, Bronk Ramsey C, Butzin M, Cheng H, Edwards RL, Friedrich M, Grootes PM, Guilderson TP, Hajdas I, Heaton TJ, Hogg AG, Hughen KA, Kromer B, Manning SW, Muscheler R, Palmer JG, Pearson C, van der Plicht J, Reimer RW, Richards DA, Scott EM, Southon JR, Turney CSM, Wacker L, Adolphi F, Büntgen U, Capano M, Fahrni SM, Fogtmann-Schulz A, Friedrich R, Köhler P, Kudsk S, Miyake F, Olsen J, Reinig F, Sakamoto M, Sookdeo A, Talamo S (2020) The IntCal20 northern hemisphere radiocarbon age calibration curve (0–55 cal kBP). Radiocarbon 62:725–757. https://doi.org/10.1017/RDC.2020.41

Richmond B, Szczuciński W, Chagué-Goff C, Goto K, Sugawara D, Witter R, Tappin DR, Jaffe B, Fujino S, Nishimura Y, Goff J (2012) Erosion, deposition and landscape change on the Sendai coastal plain, Japan, resulting from the March 11, 2011 Tohoku-oki tsunami. Sediment Geol 282:27–39. https://doi.org/10.1016/j.sedgeo.2012.08.005

Sabatier P, Dezileau L, Colin C, Briqueu L, Bouchette F, Martinez P, Siani G, Raynal O, Von Grafenstein U (2012) 7000 years of paleostorm activity in the NW Mediterranean Sea in response to Holocene climate events. Quat Res 77:1–11. https://doi.org/10.1016/j.yqres.2011.09.002

Scheffers A, Kelletat D, Vött A, May SM, Scheffers S (2008) Late Holocene tsunami traces on the western and southern coastlines of the Peloponnesus (Greece). Earth Planet Sci Lett 269:271–279. https://doi.org/10.1016/j.epsl.2008.02.021

Schulmeister MK, Butler JJ, Healey JM, Zheng L, Wysocki DA, McCall GW (2003) Direct-push electrical conductivity logging for high-resolution hydrostratigraphic characterization. Groundw Monit Remediat 23:52–62. https://doi.org/10.1111/j.1745-6592.2003.tb00683.x

Shaw B, Ambraseys NN, England PC, Floyd MA, Gorman GJ, Higham TFG, Jackson JA, Nocquet J-M, Pain CC, Piggott MD (2008) Eastern Mediterranean tectonics and tsunami hazard inferred from the AD 365 earthquake. Nat Geosci 1:268–276. https://doi.org/10.1038/ngeo151

Sordinas A (1969) Investigations of the prehistory of Corfu during 1964-1966. Balkan Stud 10:394–424

Sorensen RM (2010) Basic coastal engineering, 3rd edn. Springer, New York, p 344

Soukissian T, Hatzinaki M, Gerasimos K, Papadopoulos A, Kallos G, Anadranistakis M (2007) Wind and wave atlas of the Hellenic Seas. Hellenic Centre for Marine Research, Athens

Stiros SC (2001) The AD 365 Crete earthquake and possible seismic clustering during the fourth to sixth centuries AD in the Eastern Mediterranean: a review of historical and archaeological data. J Struct Geol 23:545–562. https://doi.org/10.1016/S0191-8141(00)00118-8

Stiros SC (2010) The 8.5+ magnitude, AD365 earthquake in Crete: coastal uplift, topography changes, archaeological and historical signature. Quat Int 216:54–63. https://doi.org/10.1016/j.quaint.2009.05.005

Stiros SC, Drakos A (2006) A fault-Model for the Tsunami-Associated, Magnitude ≥ 8.5 Eastern Mediterranean, AD 365 Earthquake. Zeitschrift Für Geomorphol 146:125–137

Switzer AD, Bristow CS, Jones BG (2006) Investigation of large-scale washover of a small barrier system on the southeast Australian coast using ground penetrating radar. Sediment Geol 183:145–156. https://doi.org/10.1016/j.sedgeo.2005.09.015

Van Ormondt M, Nederhoff K, Van Dongeren A (2020) Delft dashboard: a quick set-up tool for hydrodynamic models. J Hydroinformatics 22:510–527. https://doi.org/10.2166/hydro.2020.092

van Rijn LC (1993) Principles of sediment transport in rivers, estuaries and coastal seas. Aqua Publications, Amsterdam, p 675

Viscarra Rossel RA, Minasny B, Roudier P, McBratney AB (2006) Colour space models for soil science. Geoderma 133:320–337. https://doi.org/10.1016/j.geoderma.2005.07.017

Vött A, Bareth G, Brückner H, Lang F, Hadler H, Ntageretzis K, Willershäuser T (2011a) Olympia's harbour site Pheia (Elis, Western Peloponnese, Greece) destroyed by tsunami impact. Erde 142:259–288

Vött A, Brückner H, Brockmüller S, Handl M, May SM, Gaki-Papanastassiou K, Herd R, Lang F, Maroukian H, Nelle O, Papanastassiou D (2009b) Traces of Holocene tsunamis across the Sound of Lefkada, NW Greece. Glob Planet Change 66:112–128. https://doi.org/10.1016/j.gloplacha.2008.03.015

Vött A, Brüückner H, May M, Lang F, Brockmüüller S (2007) Late Holocene tsunami imprint at the entrance of the Ambrakian gulf (NW Greece). Mééditerranéée 43–57. https://doi.org/10.4000/mediterranee.164

Vött A, Brückner H, May M, Lang F, Herd R, Brockmüller S (2008) Strong tsunami impact on the Bay of Aghios Nikolaos and its environs (NW Greece) during Classical-Hellenistic times. Quat Int 181:105–122. https://doi.org/10.1016/j.quaint.2007.02.017

Vött A, Brückner H, May SM, Sakellariou D, Nelle O, Lang F, Kapsimalis V, Jahns S, Herd R, Handl M, Fountoulis I (2009a) The Lake Voulkaria (Akarnania, NW Greece) palaeoenvironmental archive a sediment trap for multiple tsunami impact since the mid-Holocene. Z Geomorphol 53(Suppl Issue):1–37. https://doi.org/10.1127/0372-8854/2009/0053S1-0001

Vött A, Bruins HJ, Gawehn M, Goodman-Tchernov BN, De Martini PM, Kelletat D, Mastronuzzi G, Reicherter K, Röbke BR, Scheffers A, Willershäuser T, Avramidis P, Bellanova P, Costa PJM, Finkler C, Hadler H, Koster B, Lario J, Reinhardt E, Mathes-Schmidt M, Ntageretzis K, Pantosti D, Papanikolaou I, Sansò P, Scicchitano G, Smedile A, Szczuciski W (2019) Publicity waves based on manipulated geoscientific data suggesting climatic trigger for majority of tsunami findings in the Mediterranean—response to "Tsunamis in the geological record: making waves with a cautionary tale from the Mediterranean" by Marriner et al. (2017). Zeitschrift Für Geomorphol Suppl Issues 62:7–45. https://doi.org/10.1127/zfg_suppl/2018/0547

Vött A, Hadler H, Willershääuser T, Ntageretzis K, Brüückner H, Warnecke H, Grootes PM, Lang F, Nelle O, Sakellariou D (2014) Ancient harbours used as tsunami sediment traps – the case study of Krane (Cefalonia Island, Greece). In: Ladstäätter S, Pirson F, Schmidts T (eds) Häafen und Hafenstäädte im ööstlichen Mittelmeerraum von der Antike bis inbyzantinische Zeit. Neue Entdeckungen und aktuelle Forschungsansäätze. Harbors and harborcities in the eastern Mediterranean from Antiquity to the Byzantine Period: Recent discoveries and current approaches. Byzas 19, vol. II. Istanbul, pp 743–771

Vött A, Lang F, Brückner H, Gaki-Papanastassiou K, Maroukian H, Papanastassiou D, Giannikos A, Hadler H, Handl M, Ntageretzis K, Willershäuser T, Zander A (2011b) Sedimentological and geoarchaeological evidence of multiple tsunamigenic imprint on the Bay of Palairos-Pogonia (Akarnania, NW Greece). Quat Int 242:S1040618210004313. https://doi.org/10.1016/j.quaint.2010.11.002

Vött A, May M, Brückner H, Brockmüller S (2006) Sedimentary evidence of Late Holocene Tsunami events near Lefkada Island (NW Greece). Zeitschrift Für Geomorphol 146:139–172

Vött A, May SM (2009) Auf den Spuren von Tsunamis im östlichen Mittelmeer. Geogr Rundsch 12:42–48

Werner V, Baika K, Fischer P, Hadler H, Obrocki L, Willershäuser T, Tzigounaki A, Tsigkou A, Reicherter K, Papanikolaou I, Emde K, Vött A (2018) The sedimentary and geomorphological imprint of the AD 365 tsunami on the coasts of southwestern Crete (Greece)—examples from Sougia and Palaiochora. Quat Int 473:66–90. https://doi.org/10.1016/j.quaint.2017.07.016

Werner V, Baika K, Tzigounaki A, Reicherter K, Papanikolaou I, Emde K, Fischer P, Vött A (2019a) Extreme wave events recorded in sedimentary archives of the Geropotamos River (north-central Crete, Greece). Zeitschrift Für Geomorphol Suppl Issues 62:63–100. https://doi.org/10.1127/zfg_suppl/2019/0602

Werner V, Baika K, Tzigounaki A, Reicherter K, Papanikolaou I, Emde K, Fischer P, Vött A (2019b) Mid-Holocene tectonic geomorphology of northern Crete deduced from a coastal sedimentary archive near Rethymnon and a Late Bronze Age Santorini tsunamite candidate. Geomorphology 326:167–189. https://doi.org/10.1016/j.geomorph.2018.09.017

Willershäuser T, Vött A, Brückner H, Bareth G, Nelle O, Nadeau M-J, Hadler H, Ntageretzis K (2013) Holocene tsunami landfalls along the shores of the inner Gulf of Argostoli (Cefalonia Island, Greece). Z Geomorphol 57(Suppl. Iss.):105–138. https://doi.org/10.1127/0372-8854/2013/S-00149

Willershäuser T, Vött A, Hadler H, Fischer P, Röbke B, Ntageretzis K, Emde K, Brückner H (2015a) Geoscientific evidence of tsunami impact in the Gulf of Kyparissia (western Peloponnese, Greece). Z Geomorphol 59(Suppl Iss):43–80. https://doi.org/10.1127/zfg_suppl/2014/S-00189

Willershääuser T, Vöött A, Hadler H, Ntageretzis K, Emde K, Brüückner H (2015b) Holocene palaeotsunami imprints in the stratigraphical record and the coastal geomorphology of the Gialova Lagoon near Pylos (southwestern Peloponnese, Greece). Z füür Geomorphologie Suppl Issue 59:215–252. https://doi.org/10.1127/zfg_suppl/2014/S-00190

Yolsal S, Taymaz T, Yalçiner AC (2007) Understanding tsunamis, potential source regions and tsunami-prone mechanisms in the Eastern Mediterranean. SP 291:201–230. https://doi.org/10.1144/SP291.10

Authors and Affiliations

Tina Georg[1,2] · Björn R. Röbke[3] · Peter Fischer[1] · Peter Frenzel[4] · Kalliopi Baika[5] · Timo Willershäuser[1] · Andreas Vött[1]

✉ Tina Georg
tina.georg@uni-mainz.de

[1] Institute of Geography, Johannes Gutenberg-Universität Mainz, Johann-Joachim-Becher-Weg 21, 55099 Mainz, Germany

[2] Institute of Neotectonics and Natural Hazards, RWTH Aachen University, Lochnerstrasse 4–20, 52056 Aachen, Germany

[3] Department for Applied Morphodynamics, Deltares, Boussinesqweg 1, 2629 HV Delft, The Netherlands

[4] Institute of Geosciences, Friedrich Schiller University, Burgweg 11, 07749 Jena, Germany

[5] Centre Camille-Jullian, CNRS, Aix-Marseille Université, Maison Méditerranéenne des Sciences de l'Homme, 5 Rue Château de l'Horloge, 13090 Aix-en-Provence, France